FORUM GEOGRAFI
ISSN: 0852-0682 | E-ISSN: 2460-3945

HTTPS://JOURNALS.UMS.AC.ID/INDEX.PHP/FG/

Research article

Characteristics of Precipitable Water Vapor of Mesoscale Convective System During Heavy Rainfall over Greater Jakarta, Indonesia, March 3-4 2025

Prasetyo Umar Firdianto[1,2*], Bagus Satrio Wicaksono[1], Asep Adang Supriyadi[3], Nanang Yulian[4], Bangun Muljo Sukojo[1], Danang Eko Nuryanto[5]

[1] Geospatial Laboratory, Department of Geomatics Engineering, Sepuluh Nopember Institute of Technology, ITS Campus Sukolilo, Surabaya, Jawa Timur, Indonesia; [2] Meteorological Station of Tanjung Perak, Indonesia Agency of Meteorology Climatology and Geophysics (BMKG), Kalimas Baru No. 97B Port of Tanjung Perak, Surabaya, Jawa Timur, Indonesia; [3] Department of Sensing Technology, Republic of Indonesia Defence University, Area of Indonesia Peace and Security Centre (IPSC) Sentul, Bogor, Jawa Barat, Indonesia; [4] Department of Defence Science, Republic of Indonesia Defence University, Area of Indonesia Peace and Security Centre (IPSC) Sentul, Bogor, Jawa Barat, Indonesia; [5] Indonesia Agency of Meteorology Climatology and Geophysics (BMKG), Angkasa I No. 2, Kemayoran, Jakarta Pusat, Indonesia.

*) Correspondence: prasetyo.firdianto@bmkg.go.id

Citation:
Firdianto, P. U., Wicaksono, B. S., Supriyadi, A. A., Yulian, N., Sukojo, B. M., Nuryanto, D. E. (2026). Characteristics of Precipitable Water Vapor of Mesoscale Convective System During Heavy Rainfall over the Greater Jakarta 3-4 March 2025. Forum Geografi. 37(2), 108-128.

Article history:
Received: 17 January 2026
Revised: 2 March 2026
Accepted: 2 March 2026
Published: 5 March 2026

Abstract

Across the Indonesian Maritime Continent, pronounced convective activity frequently initiates cloud systems that can further organize and evolve into mesoscale convective system (MCS). This triggers extreme weather and flash flooding; for example, on March 3-4, 2025 in Greater Jakarta. This study investigates the impact of such systems on precipitable water vapor (PWV) using GNSS observations, the ERA5 reanalysis model, and Himawari satellite data. The datasets include rainfall observations, GNSS RINEX data, ERA5 reanalysis, GPM satellite precipitation, and brightness temperature from Himawari-8 channel 8. Analysis was conducted on spasiotemporal variability, timeseries, scatter plots, boxplots, bias, MAE, RMSE standard deviation, correlation, and coefficients of determination. The results indicate that PWV exhibits marked fluctuations that align with the MCS period. The distance of observation and MCS track have a significant influence on modulating PWV, whereas PWV has a weak correlation with MCS intensity. Consistent fluctuations were detected in both the GNSS and ERA5 derived PWV, although GNSS demonstrated higher sensitivity in describing PWV fluctuation compared to ERA5. Variation in brightness temperature in the upper-level moisture demonstrate patterns consistent with PWV, athough the correlation remains weak. MCSs lead to enhanced rainfall, which can trigger extreme weather conditions and flash flooding.

Keywords: Mesoscale Convective System; Precipitable Water Vapor; GNSS; Extreme rainstorm; Heavy rainfall.

1. Introduction

The Indonesian Maritime Continent (IMC) is a prominent tropical region noted for its intense and persistent convective activity (Aslam, 2025; Trismidianto *et al.,* 2024), with East Java being no exception. Such pronounced convective activity promotes the development of convective clouds, which can further consolidate and evolve into mesoscale convective systems (MCSs). Deep convective processes in tropical oceanic regions involve multiple cumulonimbus clouds founded on an anvil of cirrus clouds with a high-level outflow (Pilewskie & L'Ecuyer, 2025; Stephens *et al.,* 2024; Wang & Yuan, 2025).

According to Maddox (1980), MCSs which form in tropical regions generally exhibit either circular or linear organizational structures. The systems are commonly characterized by several physical parameters, including cloud size area, cloud shield temperature, cold cloud temperature, shape eccentricity, duration and evolution phase. Such characteristics are fundamental for identifying and classifying MCSs, particularly in satellite-based observations. However, these physical attributes are not invariant and may be significantly modified by regional environmental conditions, such as atmospheric thermodynamic instability, moisture availability, vertical wind shear, and large-scale circulation patterns, as well as by the timing of system development. Recent studies have demonstrated that both regional variability and temporal factors play a critical role in shaping MCS morphology, thermal structure and evolution, resulting in diverse MCS characteristics across different tropical environments (Angulo-Umana & Kim, 2023; Du *et al.,* 2025; Hermawan *et al.,* 2025).

MCSs are major drivers of hydro-meteorological disasters in tropical regions. Their development and persistence are frequently associated with severe storms and prolonged rainfall ranging from heavy to extreme intensity, which significantly increases the risk of surface runoff and hydrological extremes (Djakouré *et al.,* 2024; Wang *et al.,* 2023). In addition to intense precipitation, MCSs can generate strong convective winds and gust fronts capable of causing widespread damage (Cheng *et al.,* 2023), as well as enhanced ocean–atmosphere interactions that contribute to the formation of high waves, particularly in coastal and offshore environments (Du *et al.,* 2025).

As a result, MCS events often act as a primary trigger for a succession of natural hazards, including inland flooding (Atiah *et al.,* 2023; Ding *et al.,* 2024; Nuryanto *et al.,* 2021), coastal tidal flooding, landslides and structural damage (Harjana *et al.,* 2023). These impacts not only threaten lives and infrastructure, but also significantly disrupt socioeconomic activities, highlighting the critical importance of improved MCS monitoring, characterization and early warning systems.

On March 3–4, 2025, heavy rainfall occurred in the Greater Jakarta area (Jabodetabek: Jakarta, Bogor, Depok and Bekasi), which was attributed to MCS. The rainfall intensity increased significantly, reaching a peak of >40 mm/3 hours. According to BNPB (2025), the event led to major flooding on Bekasi and resulted in substantial multi-sectoral impacts in Jabodetabek, as detailed in Tables 1, 2 and 3.

Table 1. Affected Categories on Bekasi (BNPB, 2025).

Impact Category	Bekasi City	Bekasi Region
Submerged Houses	26,887	23,505
Fatalities	1	0
Displaced Persons	4,210	670
Affected Persons	83,149	88,282

Table 2. Damage and Loss by Sector (BNPB, 2025).

Damage and Loss	Total Nominal Value
Damage and Loss in the Housing Sector	Rp 1,344,732,352,500,-
Damage and Loss in the Infrastructure Sector	Rp 155,997,582,000,-
Loss in the Social Sector	Rp 36,786,198,314,-
Damage in the Economic Sector	Rp 130,275,000,000,-
Loss due to Decline in Economic Activity	Rp 14,188,511,000,-

Table 3. Losses by Region (BNPB, 2025).

Region	Total Nominal Value
Bekasi City	Rp 878,600,000,000,-
Bekasi Regency	Rp 680,000,000,000,-
DKI Jakarta	Rp 1,920,000,000,-
Depok City	Rp 28,800,000,000,-
Bogor Regency	Rp 96,700,000,000,-
Tangerang Regency	Rp 5,000,000,000,-

Approaches used to identify MCSs remain scarce and not widely developed. Whitehall *et al.* (2015a) introduced the Grab 'Em Tag 'Em Graph 'Em (GTG) algorithm as a framework for identifying and analyzing MCSs. The algorithm has been employed in several previous studies to examine MCSs associated with intense precipitation and flood-producing events across Indonesia (Hermawan *et al.,* 2025; Nuryanto *et al.*, 2019; Putri *et al.,* 2017). It effectively captures the complex evolution of MCSs by enabling the concurrent merging of multiple convective cells within a single temporal interval. A more recent method for MCS identification is PyFLEXTRKR (Feng *et al.,* 2023). One of its functionalities utilizes brightness temperature and precipitation feature data to track the cold cloud shield (CCS) and the associated MCS precipitation. This algorithm allows the entire lifecycle of the MCS to be considered, ensuring that the precipitation produced by the MCS across all its phases can be quantified. The method can be used very effectively to identify MCS characteristics and to track its movement (Du *et al.,* 2025; Prein *et al.,* 2024; Tai *et al.,* 2024). Azka and Trilaksono (2024) employed this approach to investigate the diurnal and seasonal variability of precipitation associated with MCS and non-MCS events over Borneo Island.

MCSs significantly contribute to increased precipitation in Indonesia (Azka & Trilaksono, 2024; Crook *et al.,* 2024; Trismidianto *et al.,* 2024). According to Ismanto (2011), MCS growth areas are more frequent over oceans than land, particularly over the Indian Ocean (36%), Papua (15%), the Pacific Ocean north of Papua (13%), Kalimantan (13%), and other regions (23%). In addition, the dominant MCS movement is west to southwestward, with an average nighttime lifespan, with its maximum frequency following the seasonal radiation cycle in relation to the Asian–Australian monsoon. The highest MCS frequency demonstrates a strong relationship with negative Indian Ocean Dipole (IOD–) phases and positive El Niño-Southern Oscillation (ENSO) conditions, particularly during La Niña events (Rustiana *et al.,* 2019).

The heavy to extreme rainfall commonly produced by MCSs is strongly influenced by the amount of atmospheric moisture, with precipitable water vapor (PWV) serving as a primary diagnostic parameter (Campos *et al.,* 2023; Shoji, 2013; Yoshida *et al.,* 2025). PWV represents the vertically integrated water vapor content within an atmospheric column extending through the troposphere

(Bevis *et al.,* 1992; B. Chen & Liu, 1955; S. Wang *et al.,* 2020). It is an effective indicator parameter for observing dynamic circulation systems in the atmosphere (Benevides *et al.,* 2015; Drissi El Bouzaidi *et al.,* 2025; Jiang *et al.,* 2016; Raj *et al.,* 2004) and identifies anomalies when disturbances occur in the tropospheric layer. Therefore, PWV is a crucial component in weather analysis and prediction (Benevides *et al.,* 2015).

It can be measured using multiple observational techniques, with remote sensing approaches, such as global navigation satellite system (GNSS) observations and ECMWF Reanalysis v5 (ERA5) produced by the European Centre for Medium-Range Weather Forecasts (ECMWF) being among the most widely utilized. According to Lian *et al.,* (2023), PWV derived from radiosonde observations, and GNSS shows strong agreement in terms of correlation and temporal variability. However, because GNSS, radiosonde and ERA5 represent fundamentally different types of datasets, satellite-based remote sensing products may not perform as well as upper-air balloon observations or reanalysis data that integrate multiple sources of observations. Nevertheless, high correlation coefficients between radiosonde-derived PWV and the ERA5 reanalysis have been reported at four stations in China, with values of 0.950, 0.956, 0.972 and 0.974.

The originality and main objective of this research lie in its focus on analyzing the characteristics of PWV anomalies during an MCS period, specifically examining how PWV changes and how it evolves throughout the period, causing heavy rainfall and severe flooding in Greater Jakarta. Previous studies have examined MCS characteristics using satellite-based tracking methods (Nuryanto *et al.,* 2021; Nuryanto, Hidayat, *et al.,* 2018) and investigated PWV consistency (Zhang *et al.,* 2019) and its relationship with heavy rainfall using GNSS and reanalysis data (Geng *et al.,* 2019; Xu *et al.,* 2022), while others have focused on improving PWV estimation and its application for extreme weather analysis using ERA5-based modeling approaches and GNSS observations (Saxena & Dwivedi, 2023).

In addition, a substantial body of state-of-the-art research has demonstrated the value of GNSS-derived PWV assimilation for enhancing convective-scale precipitation and MCS forecasts, primarily over midlatitude regions and in relation to the North American monsoon system (Moker *et al.,* 2018; Risanto *et al.,* 2021, 2023; Shohan *et al.,* 2025), with further applications to tropical cyclone monitoring (Lian *et al.,* 2023). However, the sensitivity and behavior of PWV during intense MCS events over the Maritime Continent, one of the most convectively active yet data-sparse regions globally, remain insufficiently explored.

This study addresses this gap by evaluating the sensitivity and consistency of PWV derived independently from GNSS and the ERA5 reanalysis during an extreme MCS event over Indonesia, while simultaneously examining its relationship with upper-tropospheric moisture conditions obtained from Himawari-9 satellite brightness temperature observations. Furthermore, the research applies the the PyFLEXTRKR algorithm (Feng *et al.,* 2023) for MCS detection and tracking in Indonesia (Azka & Trilaksono, 2024), thereby extending the use of advanced convective tracking techniques in tropical regions. Collectively, these contributions provide new insights into moisture–convection interactions during high-impact MCS events and offer a robust framework for improving the monitoring and understanding of hydro-meteorological hazards in densely populated tropical urban areas.

2. Methods

2.1. Domain Area

The research domain area was Greater Jakarta, commonly referred to as Jabodetabek, which consists of Daerah Khusus Ibukota Jakarta, Bogor, Depok, Tangerang and Bekasi. It is considered a functional region, a classification based on its high concentrations of economic activity and population. It lies within an area of complex coastal–continental interaction. The province of Banten lies to the west, while that of West Java extends across the eastern and southern regions. The northern region is directly adjacent to the Java Sea. In addition, Sumatra Island is located to the northwest and contributes to the broader regional-scale atmospheric configuration.

The selection of cors and meteorological stations was based on the spatial extent of the study domain across Greater Jakarta, and data availability during the MCS period. The meteorological station of Serang (96737), as well as the BAKO and CJKU cors stations, were excluded from the analysis. That of Serang did not record observational data during the MCS period, thereby preventing data processing and subsequent analysis. In addition, data from the BAKO and CJKU cors stations were not accessible due to data request restrictions imposed by Badan Informasi Geospasial (BIG), the official data provider.

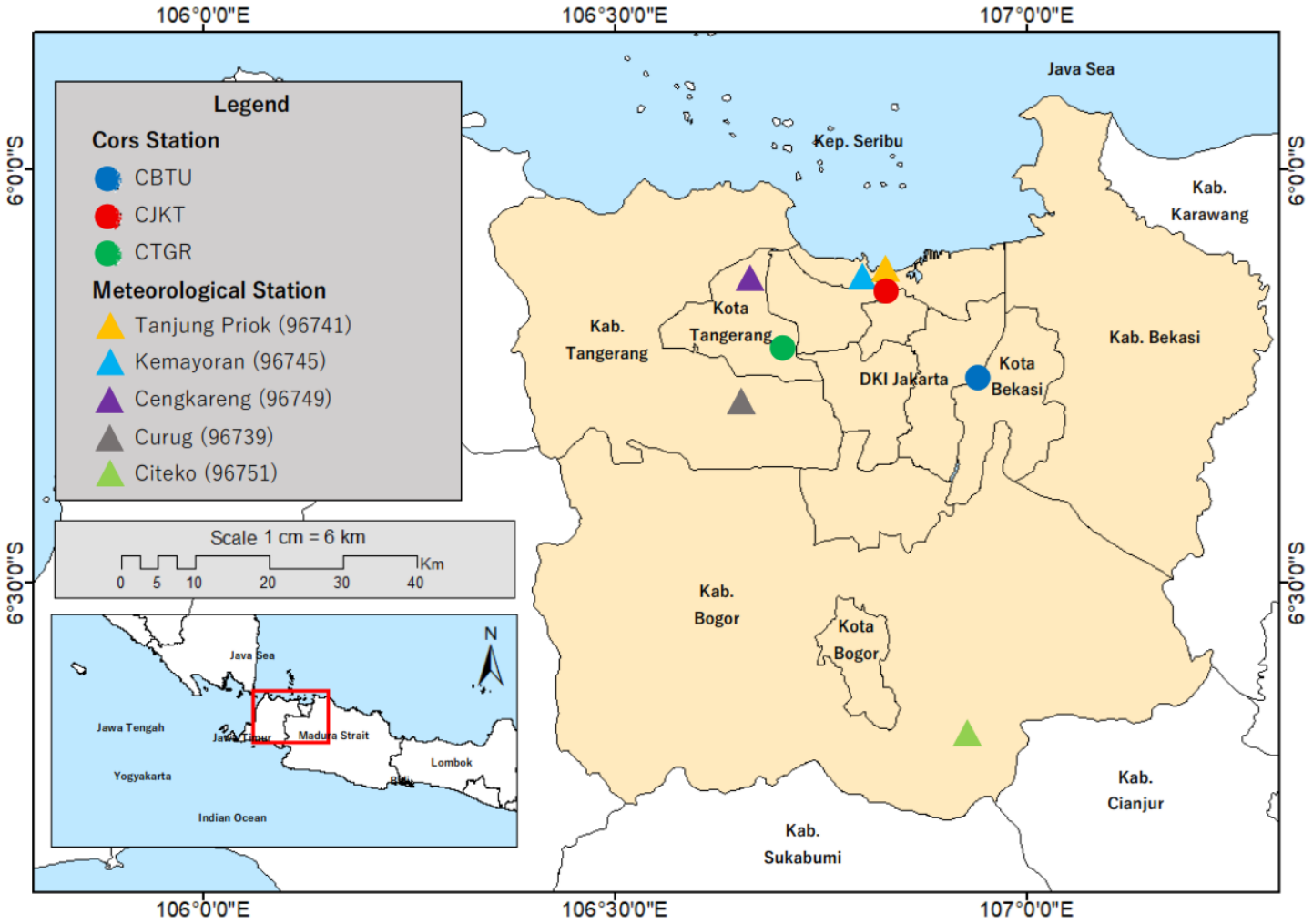

Figure 1. Domain Research Area.

Table 4. Coordinate and Elevation of Cors and Meteorological Stations.

No	Station	Latitude (°)	Longitude (°)	Elevation (m)
1	CBTU	-6.3	107.1	64.7
2	CJKT	-6.1	106.9	32.2
3	CTGR	-6.3	106.7	66.3
4	Tanjung Priok (96741)	-6.1	106.9	2.0
5	Kemayoran (96745)	-6.2	106.8	4.0
6	Cengkareng (96749)	-6.1	106.6	8.0
7	Curug (96739)	-6.2	106.6	46.0
8	Citeko (96751)	-6.7	106.9	920.0

2.2. Data

Tabular data of extreme weather and flood disasters based on BNPB (2025) are accessible at https://dibi.bnpb.go.id/. The dataset encompasses categories such as location, time, casualties, damage and losses. These data points were utilized as benchmarks to quantify the impact of intense precipitation events specifically attributed to MCS. By integrating the disaster data, our study evaluates the vulnerability and real-world consequences of MCS-driven hydrometeorological hazards.

Rainfall observation data 3h from synoptic observations of Meteorological Stations Tanjung Priok (WMO ID 96741), Cengkareng (WMO ID 96749), Kemayoran (WMO ID 96745), Curug (WMO ID 96739), and Citeko (WMO ID 96751). Databased on BMKG (2025), accessible via https://dataonline.bmkg.go.id. These data are utilized for a temporal analysis of rainfall and cloudiness at specific meteorological station points during MCS event.

Brightness temperature (Tb) data from the Global Geostationary Satellite based on Janowiak *et al.* (2017) are accessible at https://disc.gsfc.nasa.gov/. The data category selected was NCEP/CPC

L3 Half Hourly 4km Global Merged IR V1 (GPM_MERGIR). Due to the 30-minute temporal resolution, there are two data points per hour. The spectrum of the top-of-atmosphere emission is related to an equivalent temperature (Minnett & Barton, 2010), while Tb is used to identify and track convective clouds associated with events (Feng *et al.,* 2023). In addition, the precipitation feature (PF) of the Global Precipitation Measurement (GPM) mission satellite are based on Huffman *et al.* (2023). The data category selected was GPM IMERG Final Precipitation L3 Half Hourly 0.1 degree V07 (GPM_3IMERGHH). This provides rainfall estimates derived from the passive microwave (PMW) sensor using water vapor motion vectors (Jin *et al.,* 2021; Joyce & Xie, 2011). The 30-minute IMERG precipitation data are averaged to represent hourly rainfall total. According to Feng *et al.,* (2023), PF is defined as contiguous regions characterized by measurable precipitation rates to enhance convective cloud system (CCS) segmentation,with the use of hourly data considered sufficient for MCS identification.

GNSS RINEX observation data based on BIG (2025) are accessible at https://srgi.big.go.id/. The data were acquired from the following Continuously Operating Reference Stations (CORS): CBTU (Cibitung), CJKT (Tanjung Priok) and CTGR (Tangerang). The data were used to conduct a temporal analysis of PWV at CORS station points during the MCS. Model ERA5 data of specific humidity and air pressure based on ECMWF (2025) are accessible at https://cds.climate.copernicus.eu/ in NetCDF format.

The data have an hourly temporal resolution, a spatial resolution of 31 km, and 37 vertical pressure levels. The dataset was employed to analyze the PWV over the area and grid points during the MCS. Brightness temperature infrared-3 (IR-3) data from Himawari-9 satellite band 8 (wavelength bandwidth 6.2 µm) was based on BMKG (2025) via Himawari-Cast in NetCDF format. The data have a temporal resolution of 10 minutes and spatial resolution of 2 km. The dataset is able to indicate upper-level moisture atmospheric water vapor and was thus used to analyze the water vapor parameter during the occurrence of the MCS.

3.3. Method

In line with Feng *et al.,* (2023), the study employed the PyFLEXTRKR algorithm for MCS identification and tracking. This can determine the distribution and movement of convective clouds based on the temperature fields derived from satellite imagery. Fundamentally, the algorithm executes five main steps: reading input data, identifying cloud features, tracking, computing statistics, and final tracking. It monitors all convective clouds that exceed a specified minimum area threshold, which is defined based on the modified cloud-identification parameters outlined in Table 5. MCSs are then identified based on the tracked clouds.

Therefore, MCS tracking within PyFLEXTRKR encompasses the initial stage of convective cloud growth (before reaching mesoscale dimensions) through to the dissipation stage. MCS cloud trajectory is marked with a track number corresponding to the trajectory index in the track statistics file. Each track number generates a variety of final statistical variables. Various MCS types are separated using predefined criteria based on the statistical values of each track. In this study, algorithm categorization is based on MERGIR brightness temperature data and IMERG precipitation data from the GPM satellite.

Table 5. Modified Specific MCS Identification Used in the Study.

Physical Characteristics	
Cloud Tb Core and Cold	≤ 221 K (-52 ºC)
Cloud Tb Warm	≤ 241 K (-32 ºC)
Size	≥ 10^{10} m^2 (10,000 km^2)
Eccentricity	≥ 0.7
Duration	Size and temperature definition must be met for a period ≥ 6 hours
Development and Initiation	Size and temperature thresholds are first met
Termination	Size and temperature definitions are lastly satisfied
Mature	Minimum mean of cloud temperature definition must be met

The modified physical characteristics presented in Table 5, which are used as threshold inputs for PyFLEXTRKR and adjusted for the Indonesian Maritime Continent, were developed from MCS criteria proposed by Maddox (1980) and Nuryanto *et al.,* (2019). According to Maddox (1980), MCSs were identified using Tb-enhanced infrared (IR) satellite imagery from the Middle Latitude, focusing on single-cell system to as mesoscale convective complexes (MCC). Physical criteria included cloud shield with Tb ≤ 241 K (−32 °C) and areas exceeding 100,000 km², as well as interior cold cloud region with Tb ≤ 221 K (−52 °C) and areas greater than 50,000 km².

Furthermore, according to Nuryanto *et al.,* (2019), MCS identification used the GTG method Whitehall *et al.,* (2015b) to Tb IR Multi-functional Transport Satellite (MTSAT) on Tropical

Area, using physical thresholds of mean Tb ≤ 221 K (−32 °C) and a system size greater than 10,000 km². Despite methodological differences, both studies adopted common constraints of eccentricity greater than 0.7 and a minimum duration of 6 hours. Determination of PWV from the GNSS observation data is based on an algorithm developed by Geng *et al.,* (2019) using the PRIDE-PPPAR software package. PWV is derived from zenith tropospheric delay (ZTD), specifically the component categorized as zenith non-hydrostatic delay (ZNHD), which is commonly referred to as zenith wet delay (ZWD).

ZTD represents the total excess path length, or time delay, imposed on GNSS signals as they propagate through a neutral atmosphere in the vertical direction (Bevis *et al.,* 1992; Een Lujainatul Isnaini *et al.,* 2025; Lian *et al.,* 2023). This delay results from changes in the atmospheric refractive index driven by both dry gases (zenith dry delay/zenith hydrostatic delay) and water vaporZWD/ZNHD). Although ZTD introduces substantial error in high-precision GNSS positioning, it remains a fundamental parameter in meteorology for assessing the troposphere's dynamic conditions using Equation 1 and 2.

$$ZTD = ZHD + ZNHD = ZDD + ZWD \quad (1)$$

$$\mathrm{ZWD} = ZWD_{ini} + ZWD_{corr} = 10^{-6}\int_{z_o}^{\infty} N_{nh}(z)dz \quad (2)$$

where ZWDini = zenith wet delay initial (mm); ZWDcorr = zenith wet delay correction (mm); $\mathrm{N_{nh}(z)}$ = non-hydrostatic refractivity at height z.

Calculation of PWV requires a component weighted mean temperature (Tm (K)). This is a quantity defined by Davis *et al.,* (1985), derived by integrating a function of temperature and water vapor pressure profiles along the atmospheric column. In essence, Tm represents the water vapor-weighted mean temperature of the atmosphere. The specific Tm algorithm used in this study follows the Equation 3 and 4 detailed by Landskron & Böhm (2018).

$$T_m = \frac{\int_{\rho_v}(z)dz}{\int_{\rho_z}\frac{\rho_v(z)}{T(z)}dz} \quad (3)$$

$$\mathrm{PWV} = \frac{\mathrm{ZWD}\ 10^6}{\left(k_2' + \frac{k_3}{T_m}\right)R_v\rho_w} \quad (4)$$

ρ_v = water vapor density (Kg m-3); T =temperature (K); R_v= specific gas constant for water vapor (461,51 J Kg-1 K-1); ρ_w = water density (0,997 kg m-3); k_2'= refractivity constant (16,48 K mb-1); k_3= refractivity constant (3.776 K2 mb-1).

PWV ERA5 was calculated based on specific humidity and air pressure parameters across 37 levels. These values were then integrated from the surface layer up to the tropospheric boundary layer (or tropopause). The calculation algorithm utilized followed Equation 5 methodology established in research by Jiang *et al.,* (2016) and Zhang *et al.,* (2019).

$$PWV = \int_0^{p_s}\frac{q}{\rho_v\, g}dp \quad (5)$$

q = specific humidity (Kg Kg-1); p_s= surface pressure (Pa); ρ_v = water vapor density (1000 kg m-3); g = gravity (9.780325 m s2).

PWV data analysis on GNSS, ERA5 and BT Upper-level Moisture using Equation 6, 7, 8, 9, and 10 statistical method bias, mean absolute error (MAE), RMSE (root mean square error), SD (standard deviation), corr (Correlation), and R2 (Coefficient Determination).

$$\mathrm{Bias} = \frac{1}{N}\sum_{i=1}^{N}(y_i - x_i) \quad (6)$$

$$\mathrm{MAE} = \frac{1}{N}\sum_{i=1}^{N}|y_i - x_i| \quad (7)$$

$$\mathrm{RMSE} = \sqrt{\frac{1}{N}\sum_{i=1}^{N}(y_i - x_i)^2} \quad (8)$$

$$SD = \sqrt{\frac{1}{N-1}\sum_{i=1}^{N}[(y_i - x_i) - \text{Bias}]^2} \quad (9)$$

$$R = \frac{\sum_{i=1}^{N}(y_i - \bar{y})(x_i - \bar{x})}{\sqrt{\sum_{i=1}^{N}(y_i - \bar{y})^2}\sqrt{\sum_{i=1}^{N}(x_i - \bar{x})^2}} \quad (10)$$

N = total data; x_i= PWV GNSS (mm); y_i= PWV ERA5 (mm) or BT upper-level moisture (K); $\bar{x}$ = mean of PWV GNSS; $\bar{y}$ = mean of PWV ERA5 or BT upper-level moisture.

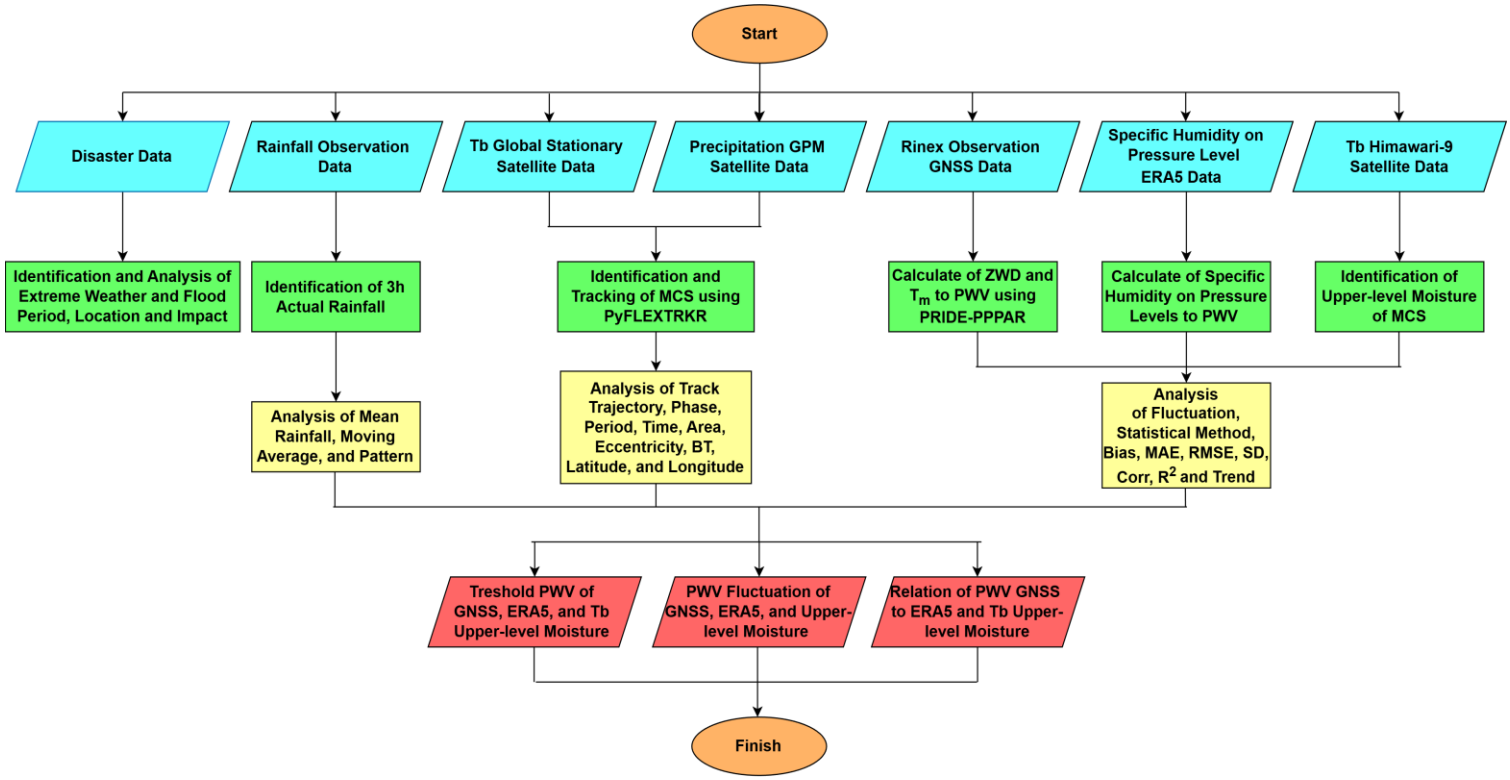

Figure 2. Research Flowchart.

3. Results and Discussion

3.1. Rainfall Observation

Figure 3 illustrates the observed rainfall data collected by rain gauges at the meteorological stations. Measurements were taken every three hours, adhering to the standard synoptic observation procedure. A total of five stations were utilized, each identified by its WMO ID number. They are distributed across the Greater Jakarta area (Jabodetabek), with their locations detailed in Figure 1 and Table 4.

Table 6. Rainfall Observation Statistics.

Rainfall	Tanjung Priok (mm)	Kemayoran (mm)	Cengkareng (mm)	Curug (mm)	Citeko (mm)
Max (mm)	42.0	27.0	23.0	18.8	42.0
Hour (UTC)				15.00-18.00	09.00-12.00; 15.00-18.00

Table 6 presents the statistical values. The maximum rainfall peak across all stations occurred between 15:00 and 18:00 UTC, with the absolute highest maximum rainfall recorded of 42.0 mm at both Tanjung Priok and Citeko stations. The overall average maximum rainfall across all stations was 30.6 mm, which is classified as heavy rainfall. The observed rainfall fluctuations demonstrated significant increases and decreases, forming a unimodal peak pattern across all stations. This pattern is clearly reflected in the trend line, which represents the moving average.

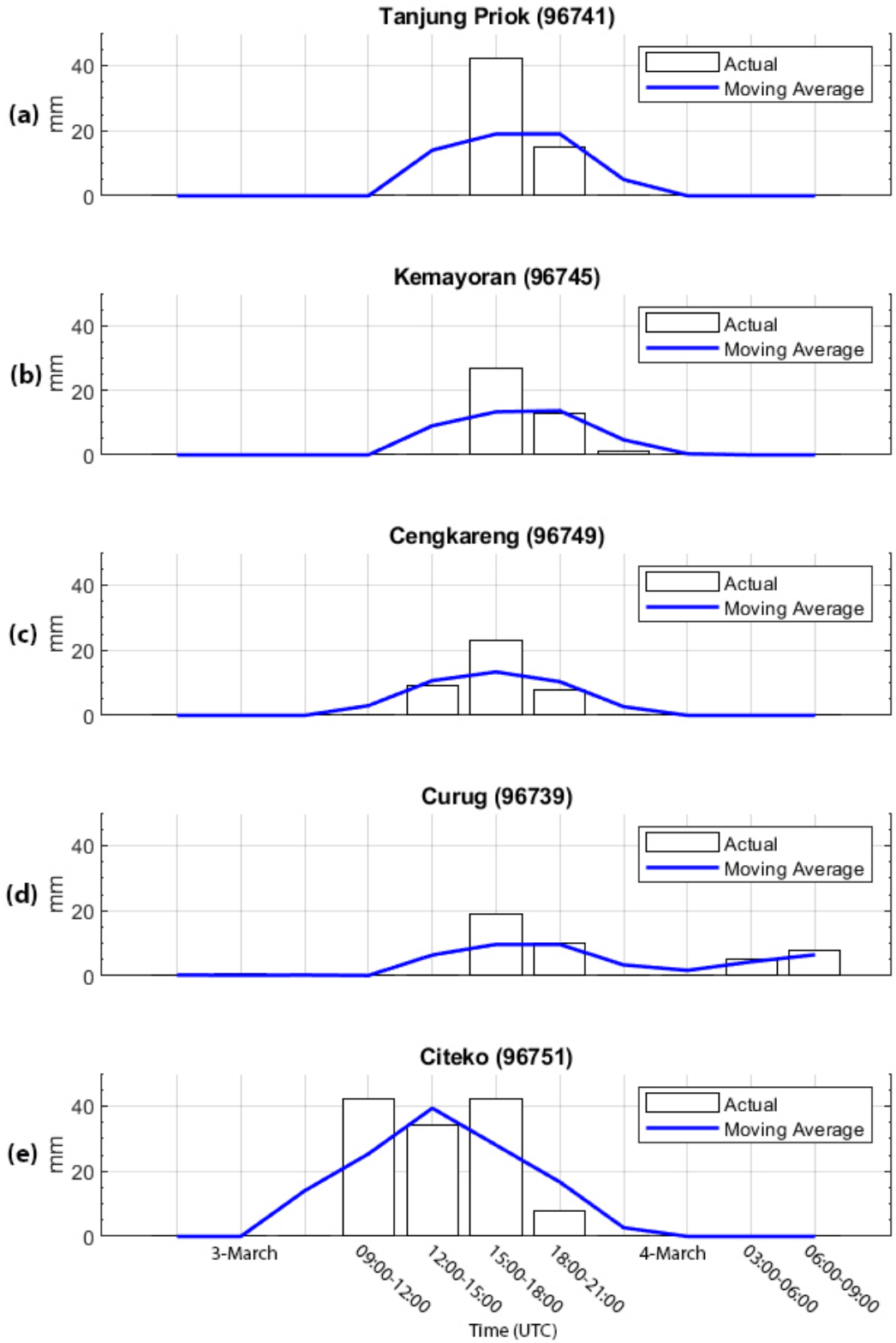

Figure 3. Rainfall Observations every 3 hours During Heavy Rainfall at the Meteorological Stations of (a) Tanjung Priok, (b) Kemayoran, (c) Cengkareng, (d) Curug and (e) Citeko.

3.2. MCS Characteristics Based on PyFLEXTRKR in Greater Jakarta

During heavy rainfall over Jabodetabek, analysis of the convective cloud system was conducted using the PyFLEXTRKR method with the Tb Global Geostationary satellite and Pf GPM satellite. The results are presented in Table 7 and Figures 4-5. Table 7 compiles the physical MCS characteristics, including phase, period, time, area, eccentricity, Tb, latitude,and longitude. Figure 4 shows further processing related to the spatiotemporal characteristics of MCS, while in Figure 5 the spatial distribution of MCS clusters during the initiation, mature and termination phases can be seen.

Table 7. MCS Characteristics Based on the Tb Global Geostationary Satellite and Pf GPM Satellite

Phase	Period (hour)	Time (UTC)	Max Area of Tb (10^{11} m^2)	Max Area of Precipitation Feature (10^{11} m^2)	Eccentricity of Precipitation Feature	Mean Tb (K)	Latitude (N)	Longtitude (E)
		09:30	0.161	0.026	0.906	211.892	-6.845	106.596
		10:30	0.177	0.032	0.956	210.333	-6.644	106.392
		11:30	0.209	0.017	0.870	212.213	-6.650	106.491
Initiation and Development		12:30	0.205	0.038	0.903	211.954	-6.671	106.754
		13:30	0.208	0.097	0.877	209.315	-6.715	107.223
		14:30	0.239	0.111	0.861	208.808	-6.705	107.150
		15:30	0.301	0.166	0.734	208.979	-6.447	106.721
		16:30	0.436	0.253	0.769	206.603	-6.347	106.452
Mature	15	17:30	0.567	0.306	0.915	206.146	-6.261	106.292
		18:30	0.878	0.306	0.950	208.115	-5.715	106.539
		19:30	1.735	0.594	0.810	208.530	-5.683	104.334
Dissipation and Termination		20:30	1.816	0.550	0.970	208.216	-5.480	104.247
		21:30	1.857	0.626	0.959	208.376	-5.377	104.275
		22:30	2.063	0.659	0.890	209.946	-5.386	104.791
		23:30	1.690	0.617	0.820	209.933	-5.338	105.967
		00:30	1.643	0.469	0.854	211.620	-5.380	105.696
Mean			0.887	0.304	0.878	209.436		
Max			2.063	0.590	0.970	212.213		
Min			0.161	0.017	0.734	206.146		

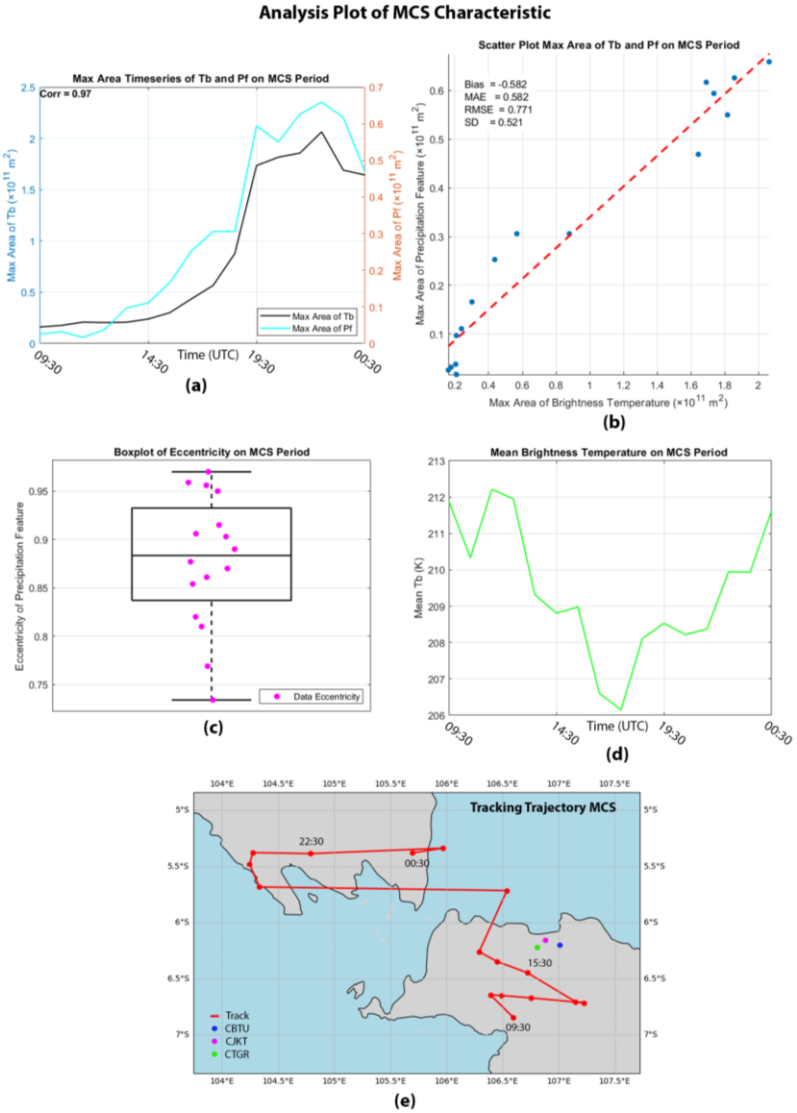

Figure 4. (a) Spasiotemporal Characteristics of MCS Period, (b) Comparison of Maximum Areas Tb and Pf, (c) Boxplot Eccentricity, (d) Timeseries Mean Tb, (e) Tracking Trajectory Based on Mean Latitude and Longitude Feature.

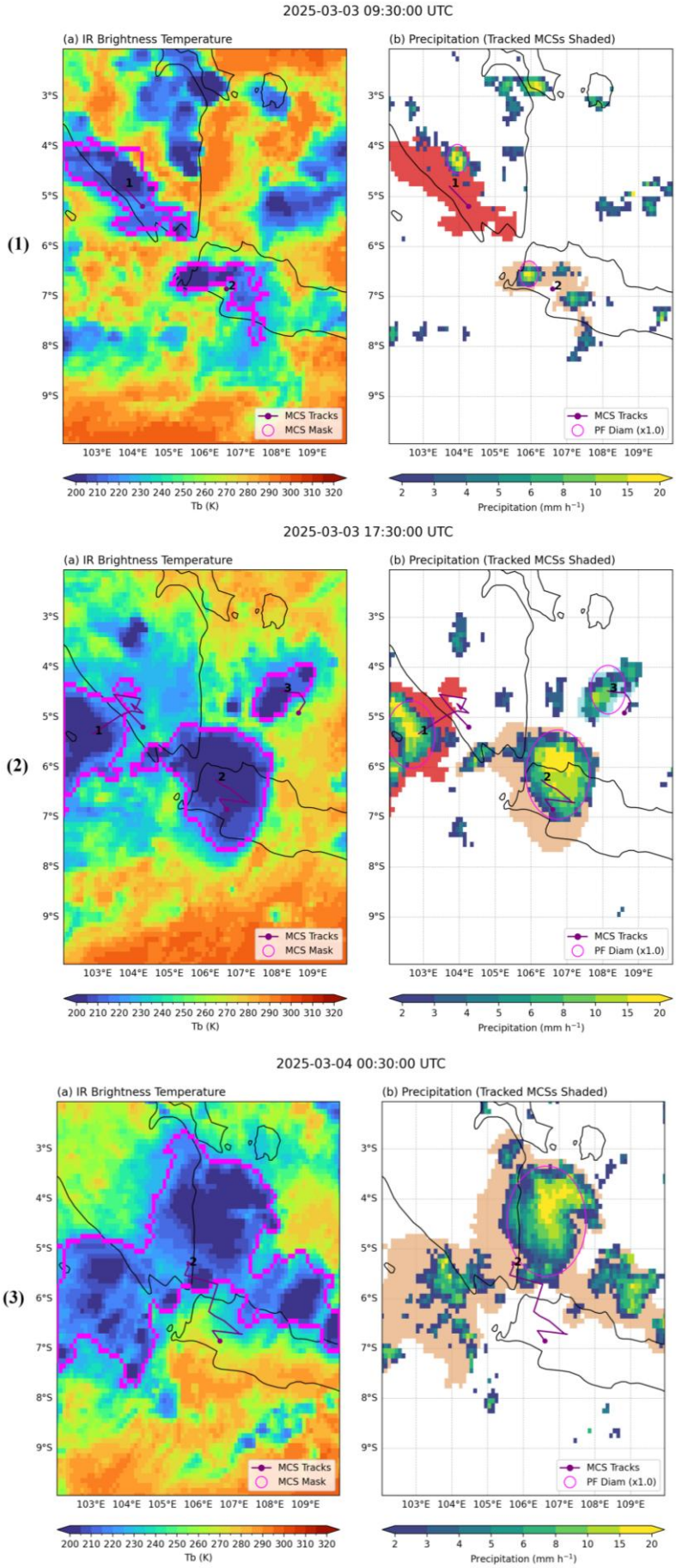

Figure 5. Spatial Distribution of MCS Based on Index Numbers Identified by the PyFLEXTRKR Method Based on IR Brightness Temperature and Precipitation Feature at (1) Beginning of Initiation, (2) Mature, and (3) End of Termination.

Table 7 shows the MCS characteristics based on Tb and Pf. The table presents phase, period, time, maximum area of Tb, maximum area of Pf, Pf eccentricity, mean Tb, latitude and longitude. The MCS demonstrated a total lifetime of 15 h, comprising a 12 h development and initiation phase, 1 hour mature phase, and 2 h dissipation and termination phase. At the beginning of the development and initiation phase, MCS exhibited a maximum Tb area of 0.161 x 1011 m^2 (16100 km^2) and a maximum Pf area of 0.026 x 1011 m^2 (2600 km^2). The system then developed into the mature phase, with the MCS reaching a maximum Tb area of 2.063 x 1011 m^2 (206300 km^2) and maximum Pf area of dan 0.659 x 1011 m^2 (65900 km^2). At the end of the termination phase, the MCS maximum Tb area was recorded as 1.643 x 1011 m^2 (164300 km^2), and maximum Pf area as 0.469 x 1011 m^2 (46900 km^2). This evolution is consistent with the temporal distribution pattern of the maximum Tb and Pf areas shown in Figure 4a, where a significant increase in area was observed during the development and initiation phase, followed by the highest peak during the mature phase, and a subsequent reduction in area during the dissipation and termination phase. Furthermore, a strong relation between the maximum Tb and Pf areas is evident, as illustrated in Figures 4a and 4b.

The spatial output of PyFLEXTRKR for MCS identification is presented in Figure 5. The MCS labeled index number 2 is the focus of this study, as it was responsible for the heavy rainfall over Jakarta. At the beginning of the initiation phase, the MCS with Tb ≤ 221 K (−52°C) only covered the Bogor and Tangerang areas, with an estimated rainfall of up to 10 mm h^{-1}. In the mature phase, the MCS covered the entire Jabodetabek area, with an estimated rainfall reaching 15 mm h^{-1}. Finally, during the termination phase, the MCS only covered the Bekasi area, with an estimated rainfall of 3 mm h^{-1}. The distribution of MCS eccentricity is shown in Figure 4c. Statistically, the eccentricity has an average of 0.878, with a maximum value of 0.970 and a minimum of 0.734. Therefore, the resulting data range is 0.236. This indicates that the MCS clouds generally had a rounded and circular shape. The tight spread of eccentricity values in the boxplot indicates low variability. The fluctuation pattern of mean Tb is presented in Figure 4d. The pattern exhibits an inverse relation compared to the data for the MCS maximum area (Figure 4a). Mean Tb reaches its peak faster than the maximum area value. Statistically, mean Tb has an average of 209.436 K (-63.564 °C), with a maximum of 212.213 K (-60.787 °C). The minimum mean Tb reached was 206.146 K (-66.854 °C). The MCS trajectory from the initiation phase to the termination phase is shown in Figure 4e. The observed trajectory moved from the southeast of West Java at 09.30 UTC and ended in Lampung, Sumatra at 00.30 UTC. It was fairly long because of its relatively long lifetime of 15 h. During the end of the termination phase shown in Figure 5c, the MCS is still observed in the brightness temperature image to have a large area. This occurs even though the cloud cells have already split when viewed from their precipitation features.

3.3. Extension of MCS Cloud Cell Evolution Based on PyFLEXTRKR in Greater Jakarta

In the following observations, the MCS cloud cell was not found to dissipate immediately, but to undergo redevelopment, as shown in Table 8 and Figures 6-7. Table 8 indicates the physical characteristics of the regenerated MCS, including phase, period, time, area, eccentricity, Tb, latitude and longitude. Figure 6 depicts the tracking trajectory of the extended MCS, while Figure 7 presents the spatial distribution of the MCS clusters during the initiation phase, representing a continued stage of cloud development from the previous MCS event. The subsequent MCS cloud cluster is identified by index number 5.

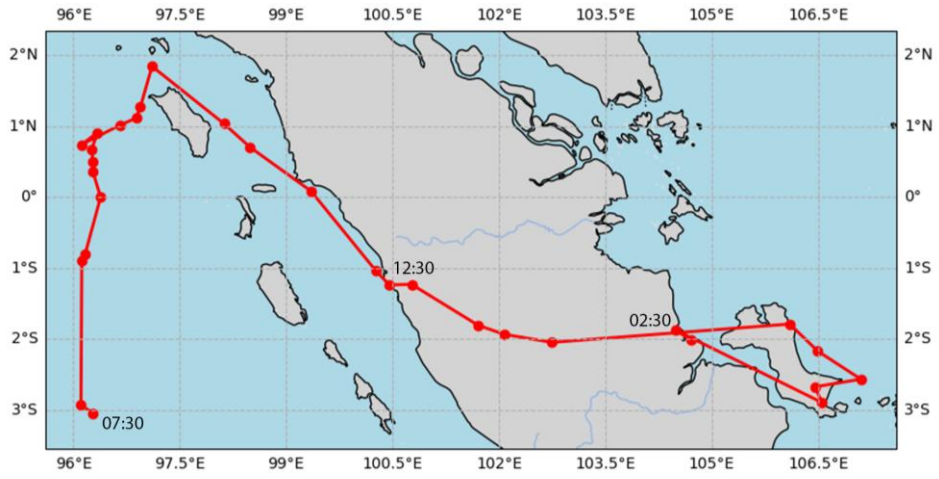

Figure 6. Tracking Trajectory of the Extension of the MCS Cloud Cell Evolution.

Table 8. Characteristics of the Extension of the MCS Cloud Cell Evolution based on the Tb Global Geostationary Satellite and PF GPM Satellite.

Phase	Period (hours)	Time (UTC)	Max Area of Tb (10^{11} m^2)	Max Area of Precipitation Feature (10^{11} m^2)	Eccentricity of Precipitation Feature	Mean Tb (K)	Latitude (N)	Longtitude (E)
		02:30	0.097	0.047	0.911	211.407	-2.011	104.705
		03:30	0.132	0.054	0.886	209.108	-1.872	104.490
		04:30	0.900	0.279	0.838	210.520	-2.891	106.554
		05:30	1.051	0.317	0.957	211.143	-2.670	106.456
Development and Initiation		06:30	1.526	0.329	0.958	211.820	-2.562	107.102
		07:30	1.952	0.285	0.960	211.979	-2.168	106.495
		08:30	2.531	0.314	0.930	211.456	-1.786	106.099
		09:30	2.026	0.387	0.968	208.625	-2.044	102.747
		10:30	2.053	0.542	0.966	206.032	-1.931	102.074
		11:30	2.143	0.497	0.989	205.702	-1.804	101.707
Mature		12:30	1.905	0.615	0.984	204.985	-1.228	100.769
		13:30	1.996	0.760	0.946	206.548	-1.235	100.454
		14:30	2.047	0.465	0.981	211.089	-1.038	100.266
		15:30	2.161	0.680	0.965	214.729	0.085	99.350
	29	16:30	0.809	0.470	0.956	211.414	0.704	98.489
		17:30	0.719	0.560	0.956	207.756	1.034	98.123
		18:30	1.139	0.809	0.970	209.450	1.841	97.109
		19:30	1.593	0.907	0.971	210.377	1.266	96.944
		20:30	1.611	0.929	0.963	210.223	1.112	96.885
Dissipation and Termination		21:30	1.635	0.124	0.947	210.796	1.013	96.656
		22:30	1.905	0.821	0.951	212.796	0.738	96.114
		23:30	2.068	0.124	0.963	211.197	0.909	96.340
		00:30	1.953	1.065	0.853	212.119	0.675	96.260
		01:30	1.747	1.152	0.962	211.400	0.493	96.275
		02:30	1.714	1.182	0.929	212.906	0.358	96.276
		03:30	1.462	1.022	0.747	214.543	0.000	96.384
		04:30	1.601	0.222	0.866	213.904	-0.800	96.167
		05:30	1.385	0.207	0.884	215.354	-0.894	96.119
		06:30	0.539	0.116	0.924	214.265	-2.928	96.107
		07:30	0.544	0.143	0.935	214.151	-3.041	96.279

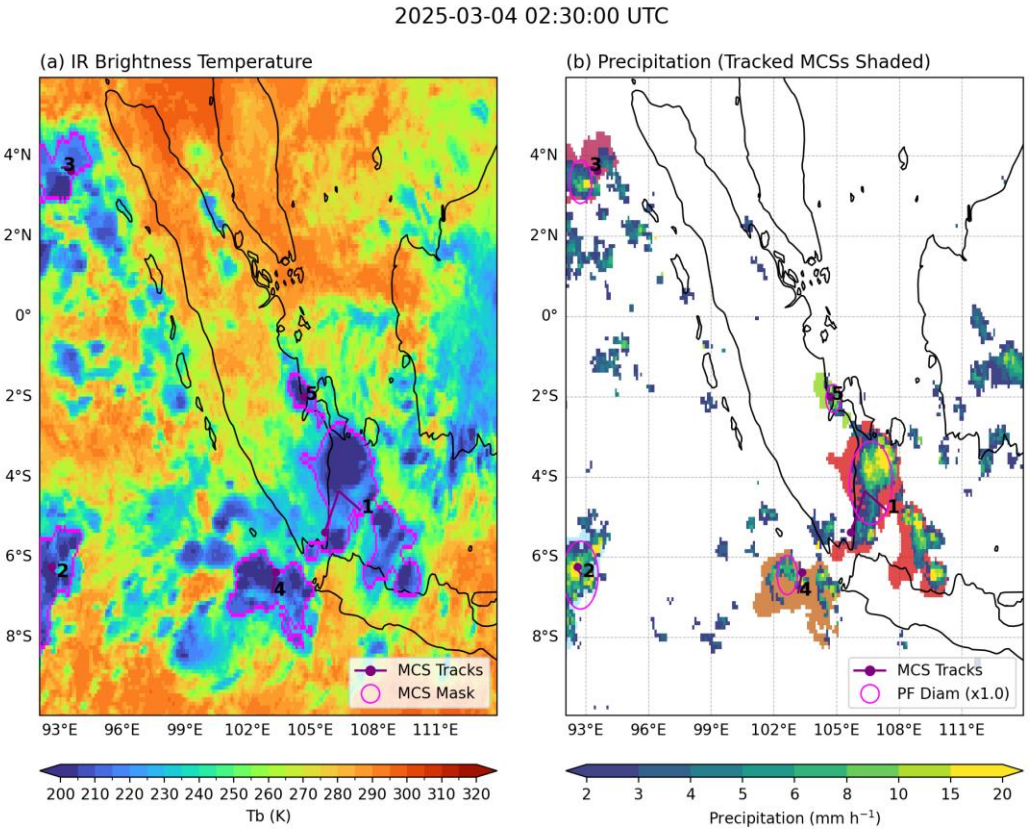

Figure 7. MCS Spatial Distribution Based on Index Numbers Identified by the PyFLEXTRKR Method Based on (a) IR Brightness Temperature and (b) Precipitation Feature at the Beginning of Development and Initiation

The MCS entered its initiation phase at 02.30 UTC. The cloud cell that had already split during the dissipation stage at 00.30 UTC developed again into an MCS. At the beginning of the initiation phase, the MCS had a maximum Tb area of 0.0097 × 10^{11} m² (970 km²), a maximum Pf area of 0.047 × 10^{11} m² (470 km²), an eccentricity of 0.911, and a mean Tb of 211.407 K (−61.593°C). The formation location was at 2.011°S, 104.705°E. In the mature phase it reached a maximum Tb area of 1.905 x 1011 m^2 (190500 km^2) and maximum Pf area of 0.615 x 1011 m^2 (61500 km^2). Although at that time the MCS had not yet reached its maximum area, the mean Tb had the lowest temperature of 204.985 K (−68.165°C). At the end of the termination phase, the maximum MCS Tb area was recorded as 0.143 x 1011 m^2 (14300 km^2) and maximum Pf area as 0.935 x 1011 m2 (93,500 km^2). The movement of the MCS can be observed in Figure 6 in the form of a track trajectory. It had a very long lifetime of 29 h.

3.4. PWV Fluctuation of GNSS and ERA5

During the MCS period, statistical analysis was conducted at each cors station using time-series and scatterplot diagrams, as shown in Figures 8 and 9. The time series diagrams in Figure 8 indicate the temporal variability of the PWV derived GNSS and ERA5. The plots facilitate identification of PWV evolution in response to MCS development and assessment of fluctuation patterns, trend consistency and their temporal correspondence. Figure 9 presents scatterplot diagrams to examine the distribution and relationship between PWV GNSS and ERA5. Each plot is complemented by statistical uncertainty, including bias, MAE, RMSE, and SD. The framework provides a comprehensive and detailed statistical evaluation of the relation between PWV GNSS and ERA5 during the MCS period.

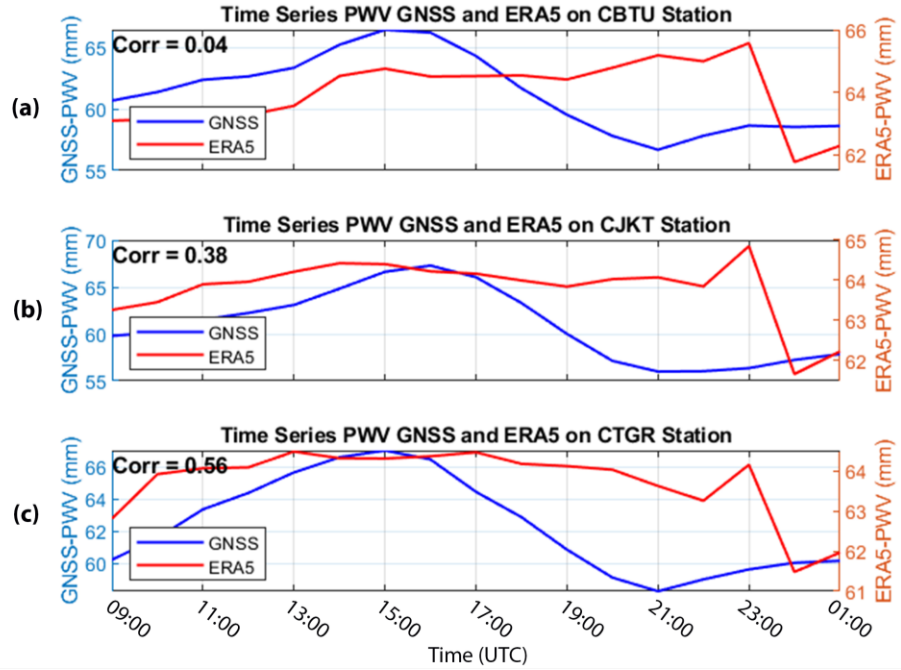

Figure 8. Comparison of Temporal Distribution of PWV GNSS and ERA5 during the MCS Period at (a) CBTU Station, (b) CJKT Station and (c) CTGR Station.

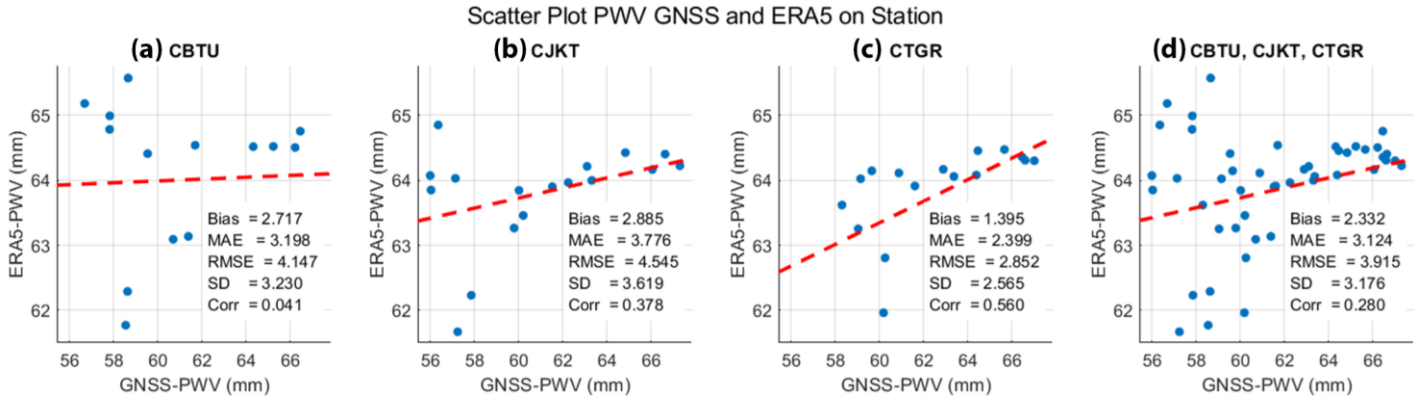

Figure 9. Scatterplot Distribution of PWV GNSS and ERA5 during the MCS Period at (a) CBTU Station, (b) CJKT Station, (c) CTGR Station and (d) Composite of CBTU, CJKT and CTGR Stations.

In the diagrams, the timescale follows the temporal resolution of the ERA5 data, available only hourly. Figure 8 shows that the GNSS and ERA5-derived PWV values gradually increased from 09.00 UTC. They then reached their highest (peak) PWV values at 15.00–16.00 UTC for GNSS and 13.00–16.00 UTC for ERA5. This corresponds to the time when the MCS center was closest to the station, at 15.30 UTC, as shown in Figure 4e. For the CBTU station (Figure 8a), the highest (peak) PWV values for GNSS and ERA5 occurred at 15.00 UTC, at 66.442 mm and 64.756 mm respectively. For the CJKT station (Figure 8b), peak PWV for GNSS occurred at 16.00 UTC at 67.289 mm, while peak PWV for ERA5 occurred at 14.00 UTC at 64.426 mm. For the CTGR station (Figure 8c), peak PWV for GNSS occurred at 15.00 UTC at 66.999 mm, while the peak PWV value for ERA5 occurred at 13.00 UTC at 64.474 mm. GNSS PWV then decreased gradually, before increasing again at 21.00 UTC, although not significantly. ERA5 PWV shows irregular increases and decreases. The PWV values increased significantly at 22.00 UTC, before decreasing significantly at 23.00 UTC.

Figure 9 shows that the relation between GNSS PWV and ERA5 PWV varied greatly during the MCS period. Correlation values were 0.041 (very low) at the CBTU station, 0.378 (low) at the CJKT station, 0.560 (moderate) at the CTGR station, and 0.280 (low) when all the stations were combined. The trend line resulting from this relation has a positive slope.

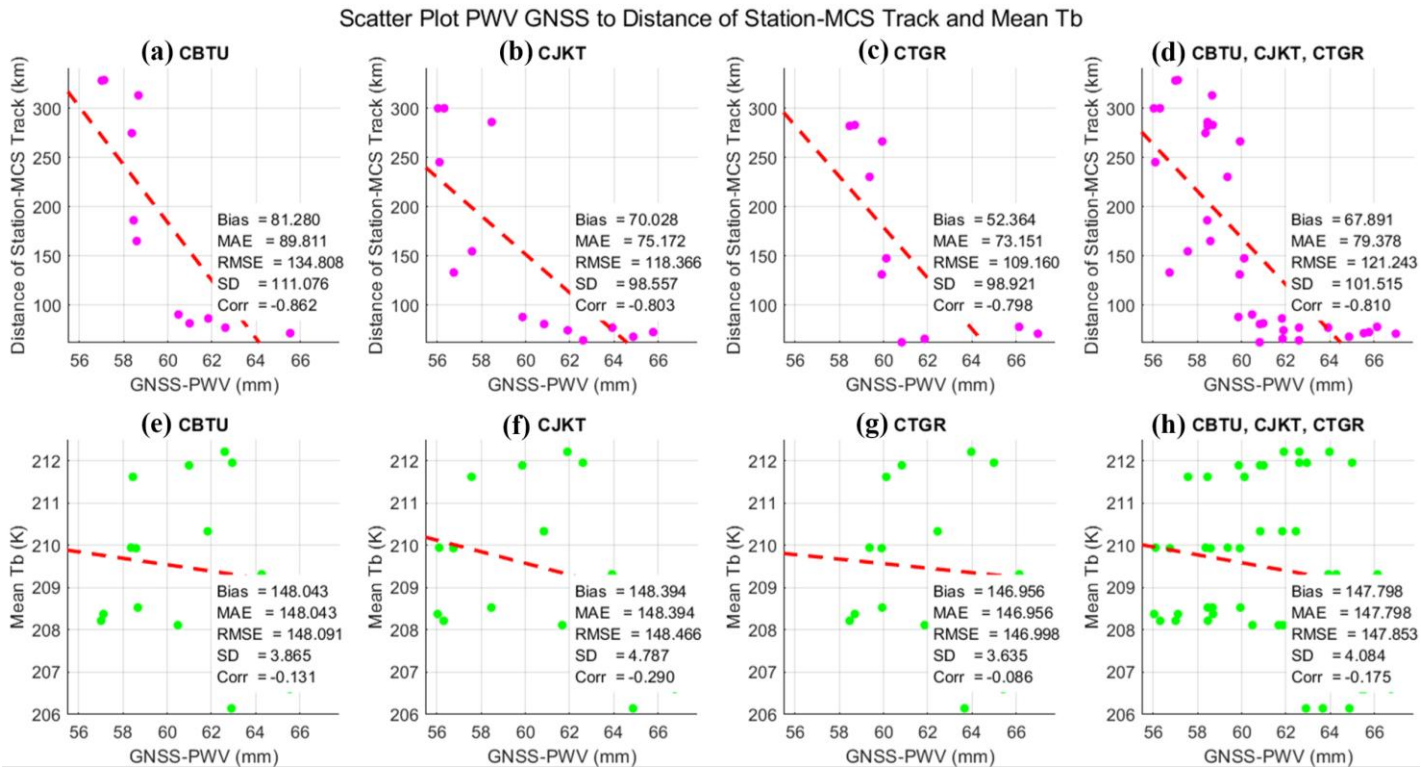

Figure 10. Scatter Plot Distribution of PWV GNSS to Distance of Station-MCS Track: (a) CBTU, (b) CJKT, (c) CTGR, (d) CBTU-CJKT-CTGR); and Mean Tb: (e) CBTU, (f) CJKT, (g) CTGR, (h) Composite of CBTU-CJKT-CTGR).

Figure 10 presents a scatterplot that illustrates the relationship between GNSS PWV and the distance between the MCS center and stations, as well as mean Tb during the evolution of the MCS. This aims to identify the factors that influence PWV changes measured at the CORS stations. Distance refers to the position (latitude and longitude) of the MCS center detected by PyFLEXTRKR, as shown in Table 7, relative to the position (latitude and longitude) of the stations shown in Table 4.

Figures 10a, 10b, 10c and 10d indicate strong to very strong correlations at each CORS station, together with a composite analysis. The correlation ranges from −0.798 to −0.862, confirming a consistently strong inverse relation between PWV GNSS and the distance from the station to the MCS track. The results demonstrate that distance is a key controlling parameter influencing PWV variability during the MCS period. A negative correlation implies that shorter distances between CORS stations and the MCS trajectory are associated with higher PWV values, whereas greater distances correspond to lower ones. This pattern reflects the enhanced moisture accumulation in proximity to the active convective system. The tendency is further supported by the time series analysis presented in Figure 11, which shows increasing PWV values as the MCS approaches the station, and decreasing ones as it moves away.

Mean Tb refers to the average brightness temperature detected by PyFLEXTRKR, as shown in Table 7. Figures 10e, 10f, 10g and 10h indicate that correlation is very weak to weak. Therefore, mean Tb has a small influence on PWV. ERA5 cannot be compared with the distance of stations to the MCS track and mean Tb because of the differences in observation times. ERA5 is available at full hour intervals, whereas PyFLEXTRKR outputs are not.

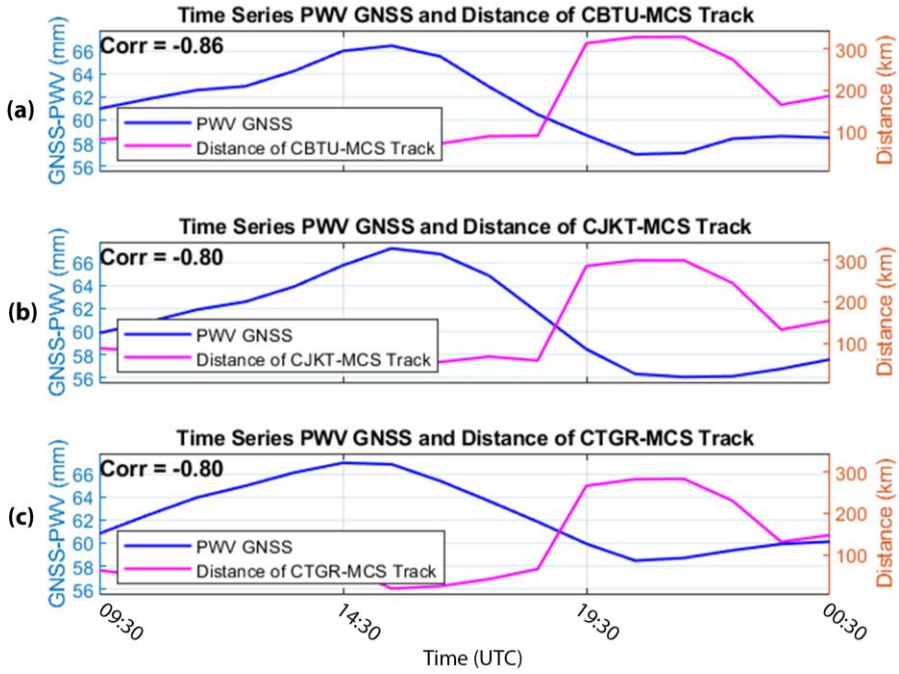

Figure 11. Comparison of Temporal Distribution of PWV GNSS and Distance of Station to MCS Track During the MCS Period at (a) CBTU station, (b) CJKT station, and (c) CTGR station

Figure 11 illustrates the timeseries relationship between PWV and distance. The results show that PWV changes follow the variations in distance that occur. Maximum PWV values are reached when the distance between the MCS and station is small. Therefore, the PWV value closely depends on the distance of the MCS from the observation location.

3.5. Comparison of PWV GNSS and Brightness Temperature Air Moisture Himawari

Figures 12, 13 and 14 present a comparison of PWV GNSS and Tb upper-level moisture. The timescale follows the temporal resolution of the Himawari satellite data, which is available every 10 minutes. The time series plots in Figure 12 illustrate the temporal variability of PWV and Tb, enabling identification of fluctuation patterns and temporal relations at each CORS station and in composite. Figure 13 shows scatterplots indicating the relation between PWV and Tb based on the composite distribution of CORS stations. Furthermore, Figure 14 shows scatterplots of each station and the composite with statistical uncertainty, including bias, MAE, RMSE and SD.

Figure 12 shows that fluctuations in GNSS PWV and BT upper-level moisture form opposite curves during the MCS period. When GNSS PWV increases as the MCS approaches the station location, Tb upper-level moisture decreases. This is indicated by negative correlation values at all CORS stations. Figure 13 presents a point distribution of PWV GNSS and Tb Upper-level moisture. The polynomial curve represents the best trend line with the highest coefficient of determination (R^2) of 0.256. This is because the R^2 values for the linear (0.077), logarithmic (0.071), power (0.070) and exponential trend lines are lower, with the exponential value being negative.

In addition, Figure 13 shows that the highest PWV values and lowest Tb upper-level moisture values occur at different times, but still within a short time interval. GNSS PWV reaches its highest (peak) value first, followed by the lowest Tb upper-level moisture value. For the CBTU station (Figure 10a), highest (peak) PWV occurs at 15:30 UTC, with a value of 66.470 mm, and the lowest upper-level moisture Tb occurs at 16:30 UTC with a value of 191.661 K (−81.489°C). For the CJKT station (Figure 10b), highest (peak) PWV occurs at 15:50 UTC with a value of 67.383 mm, and lowest BT upper-level moisture occurs at 17:00 UTC, with a value of 191.661 K (−81.489°C). For the CTGR station (Figure 10c), highest (peak) PWV occurs at 14:40 UTC with a value of 67.051 mm, and lowest Tb upper-level moisture occurs at 15:50 UTC, with a value of 189.539 K (−83.611°C).

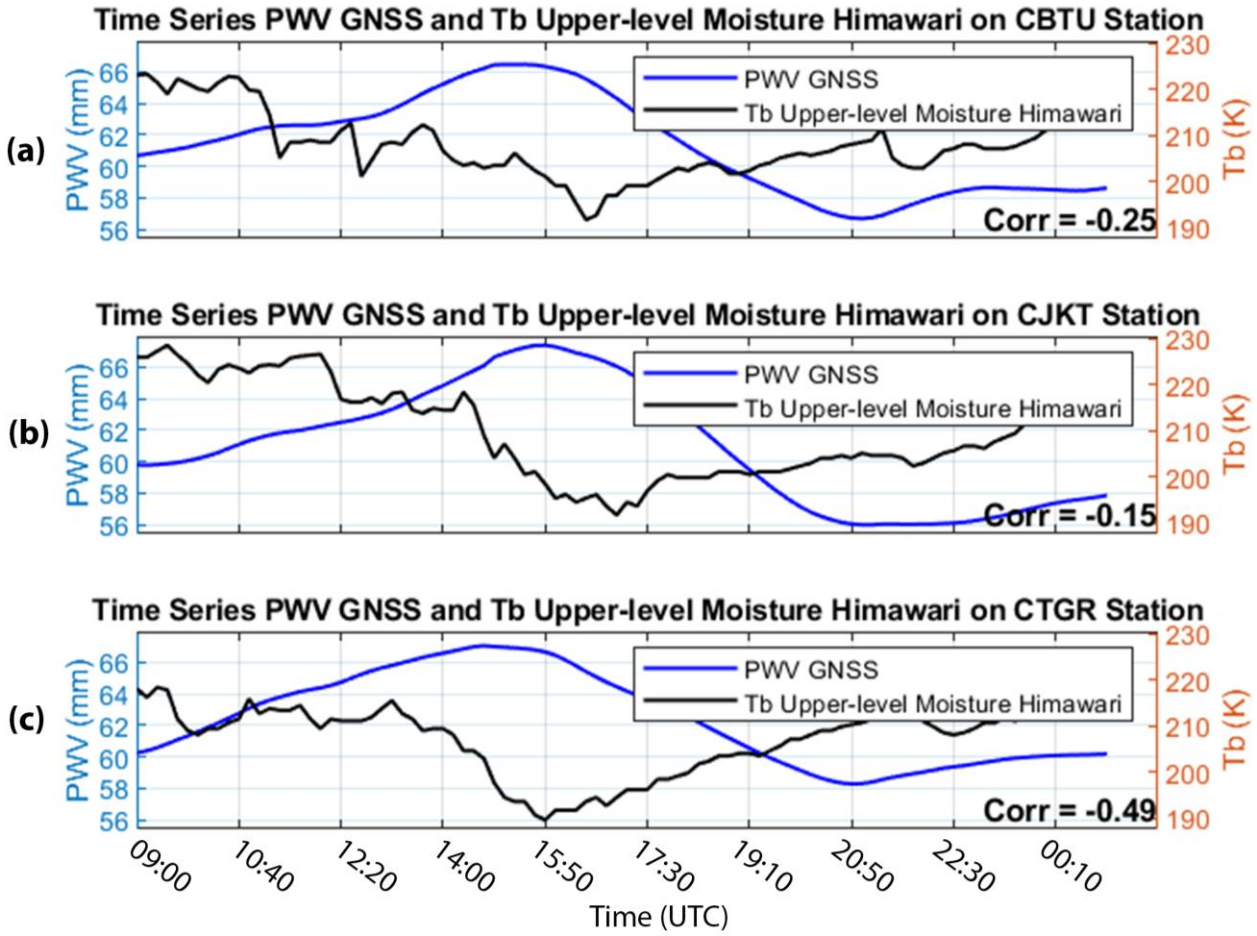

Figure 12. Comparison of Temporal Distribution of PWV GNSS and Tb Upper-level Moisture During the MCS Period at (a) CBTU Station, (b) CJKT Station and (c) CTGR Station.

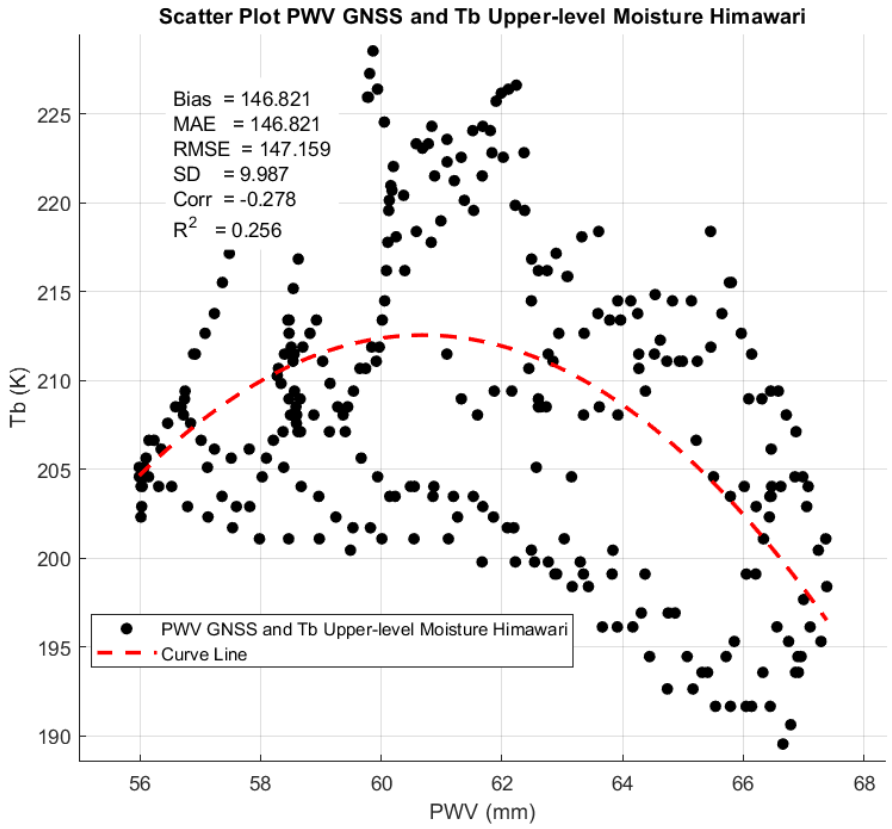

Figure 13. Scatterplot Distribution of PWV GNSS and Tb Upper-level Moisture Himawari During the MCS Period based on Composite of CBTU, CJKT and CTGR Stations.

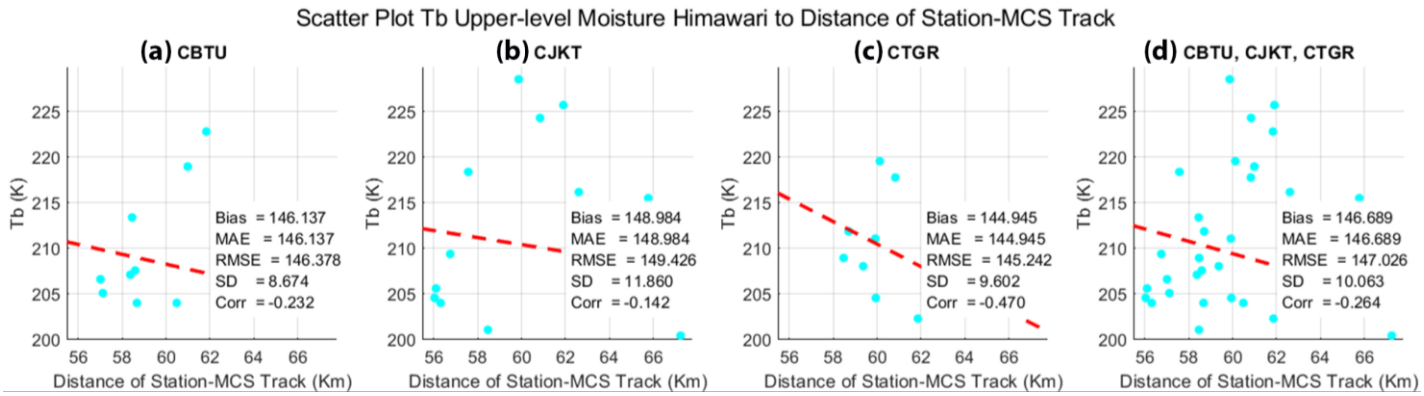

Figure 14. Scatterplot Distribution of Tb Upper-level Moisture Himawari to Distance of Station to MCS Track at (a) CBTU, (b) CJKT, (c) CTGR (d) Composite of CBTU-CJKT-CTGR.

Figure 14 presents scatterplots illustrating the relation between Tb upper-level moisture and the distance of stations to the MCS track, including each CORS station and the composite analysis. The CORS stations have weak to moderate negative correlations, with correlation coefficients of −0.232 for CBTU, −0.142 for CJKT and −0.470 for CTGR, while the combined dataset produces a correlation of −0.264. Negative slopes of the regression lines indicate that increasing station–MCS distance tends to be associated with slightly lower Tb, although the strength of this relationship remains limited. The statistical indicators also confirm this pattern, as reflected by relatively high MAE and RMSE values of approximately 145 to 149 km, which demonstrate significant dispersion of data around the regression line. Among the stations, CTGR exhibits the strongest moderate negative association, whereas CBTU and CJKT show very weak relationships. Overall, the findings indicate that variations in MCS proximity exert only a minor to moderate influence on upper-level brightness temperature at the observation locations, suggesting that other dynamical and thermodynamical processes during MCS evolution play a more dominant role in controlling BT variability.

3.6. Discussion

The rainfall observations show a significant increase in precipitation, with heavy-rain categories between 09:00 and 21:00 UTC at five meteorological stations, Tanjung Priok, Kemayoran, Cengkareng, Curug and Citeko. The rainfall fluctuations in Figure 3 represent a typical rainfall pattern associated with an MCS, namely high rainfall with heavy intensity over a long period. Maximum rainfall occurred at 15:00–18:00 UTC, during which time the MCS entered the mature phase at 17:30 UTC, with its track was closest to the Greater Jakarta area at 15:30–17:30 UTC, as shown in Figure 4e. Therefore, the MCS caused maximum impact in the Jabodetabek region. These findings align with earlier studies which have reported MCS events that generated heavy to extreme rainfall over Jakarta during other periods (Nuryanto *et al.,* 2019, 2021; Nuryanto, Hidayat, *et al.,* 2018; Nuryanto, Pawitan, *et al.*, 2018); over the western coast of Sumatra (Rais *et al.,* 2021); and in Papua (Febrizky *et al.,* 2023). In addition, MCSs have been shown to contribute significantly to rainfall enhancement across Indonesia (Azka & Trilaksono, 2024; Ismanto, 2011; Trismidianto & Satyawardhana, 2018).

The MCS characteristics show a long lifetime of 15 h. The PyFLEXTRKR method monitors MCS evolution very well, including its lifetime, phase, area, eccentricity, Tb, latitude and longitude. The maximum Tb area and maximum Pf area have a strong correlation, indicating that the method is highly effective in observing affected areas. This aligns with earlier applications of the method in Indonesia (Azka & Trilaksono, 2024; Rajagopal *et al.,* 2023). The eccentricity of MCS clouds shows consistency and persistence in their elliptical–circular shape, with values of ≥ 7. The boxplot diagram in Figure 4c shows that the eccentricity data are tightly clustered, with Q1 of 0.846 and Q3 of 0.924.

The minimum mean Tb is 206.146 K (−67.004 °C), which occurs during the mature phase at 17:30 UTC. The MCS tracking results in Figure 4e show the distance between the MCS center and observation stations, allowing for further analysis in Figures 10 and 11. The mean Tb exhibits a small difference compared to Nuryanto *et al.,* (2019), who obtained mean Tb 208 K (-65.150 oC). In addition, the movement of the MCS tends to originate in the southeast, which is associated with the Australian monsoon during that period. This finding is consistent with (Chen *et al.,* 2022; Ismanto, 2011; Ramos-Pérez *et al.,* 2022; Rustiana *et al.,* 2019). After an MCS passes its termination phase, clouds form a new system in the form of an extension of the previous MCS. The observation results in Table 8 show that the subsequent MCS had stronger characteristics and

intensity, with a lifetime of 29 hours, a maximum Tb area of 2.531 × 10^{11} m² (253,100 km²); maximum Pf area of 1.152 × 10^{11} m² (115,200 km²); maximum eccentricity of 0.984; and minimum mean Tb of 204.985 K (−68.165°C). The direction of movement tended to be from the southeast, moving across the Sumatra region.

PWV observed by GNSS and ERA5 experienced fluctuations during the MCS period, as shown in Table 8. However, the correlation is weak to moderate. Maximum correlation of PWV fluctuations between GNSS and ERA5 during the period occurs at CTGR station, with a value of 0.560. PWV fluctuations produced by GNSS have a smoother pattern. PWV shows regular increases and decreases at each time step, following the movement and evolution of the MCS. IN addition, ERA5 shows significant anomalous PWV changes at 22:00–01:00 UTC.

PWV-GNSS has a stronger relation with the distance between stations and the MCS track than with mean Tb, as shown in Figure 10. The correlation is strong to very strong. Therefore, it can be observed that fluctuations in PWV follow the distance of the MCS from the observer, as shown in Figure 11. The closer the MCS is to the observation point, the higher the PWV value; the further away the MCS is, the lower the PWV value. PWV reached its maximum value when the distance between station and MCS was shortest, at 15:30 UTC. This can be seen in the MCS tracking trajectory shown in Figure 4e. Distance therefore has a significant influence on PWV.

GNSS PWV has a moderate relation with Tb upper-level moisture, corresponding to water vapor channel 8 on the Himawari-9 satellite. A maximum correlation of 0.49 was observed at the CTGR station, as shown in Figure 12. In addition, distribution of relation value can be represented as a downward-opening curve with an R^2 value of 0.256. Therefore, BT tends to follow fluctuations in PWV that occur during the MCS period.

The correlation results relate to temporal differences between the parameters and instruments, including GNSS, ERA5, the Himawari satellite, and PyFLEXTRKR outputs. All correlations and data comparisons refer to the same time and point locations, ensuring that the datasets were equivalent and comparable.

4. Conclusion

PyFLEXTRKR effectively captures MCS evolution by identifying its characteristics, including lifetime, development phase, spatial extent, eccentricity, mean Tb, and point track location. The MCS analyzed exhibited a long lifetime of approximately 15 h, followed by an extended stage lasting up to 29 h, with a large cloud area and an elliptical-to-circular form. The mean Tb of 206.146 K (−67.004 °C) indicates a highly intense convective system, consistent with the significant rainfall and flooding impacts observed in the affected region of Greater Jakarta. PWV GNSS and ERA5 showed fluctuations during the MCS period. However, GNSS was observed to be more sensitive in measuring PWV than ERA5. This is indicated by the GNSS PWV timeseries, which exhibits a better, more regular and smoother pattern at each time step. PWV GNSS and ERA5 have a weak relationship. The relation between PWV and mean Tb was also weak, whereas PWV exhibited a strong relation with the distance between the MCS and observation stations, indicating that distance has significant influence on PWV. Tb Upper-level moisture generally followed PWV variations, although the correlations were relatively low. One limitation of the study is that PyFLEXTRKR outputs are provided at non–full-hour time intervals. As a result, the analysis of contributions of MCS distance and mean Tb to PWV was conducted using GNSS and Himawari satellite data, whereas ERA5 data could not be utilized.

Acknowledgements

The authors would like to thank the Geospatial Laboratory, Department of Geomatics Engineering, Sepuluh Nopember Institute of Technology; the Department of Defence Science and Sensing Technology, Republic of Indonesia Defence University; the Meteorological Station of Tanjung Perak; the Indonesia Agency of Meteorology Climatology, and Geophysics (BMKG); and the Geospatial Information Agency (BIG).

Author Contributions

Conceptualization: Firdianto, P. U.; **methodology**: Firdianto, P. U., Sukojo, B. M., Nuryanto, D. E.; **investigation**: Firdianto, P. U., Sukojo, B. M.; **writing—original draft preparation**: Firdianto, P. U., Sukojo, B. M., Wicaksono, B. S.; **writing—review and editing**: Firdianto, P. U., Wicaksono, B. S., Supriyadi, A. A., Yulian, N., Sukojo, B. M., Nuryanto, D. E.; **visualization**: Firdianto, P. U., Wicaksono, B. S., Supriyadi, A. A., Yulian, N., Sukojo, B. M., Nuryanto, D. E.

Conflict of interest

All authors declare that they have no conflicts of interest.

Data availability

The data supporting this study are available from the corresponding author upon reasonable request

Funding

This research was funded by Indonesia Endowment Fund for Education Agency (LPDP).

References

Angulo-Umana, P., & Kim, D. (2023). Mesoscale convective clustering enhances tropical precipitation. *Science Advances*, *9*(2), 1–9. doi: 10.1126/sciadv.abo5317

Aslam, A. A. (2025). Rainfall over the Maritime Continent: key processes, scale interactions and model representation. *Weather*, 80(6), 176–185. doi: 10.1002/wea.7731

Atiah, W. A., Amekudzi, L. K., & Danuor, S. K. (2023). Mesoscale convective systems and contributions to flood cases in Southern West Africa (SWA): A systematic review. *Weather and Climate Extremes*, 39, 100551. doi: 10.1016/j.wace.2023.100551

Azka, M. A., & Trilaksono, N. J. (2024). Comparative Analysis of Diurnal and Seasonal Variations in Precipitation of Mesoscale Convective System and Non-Mesoscale Convective System over Borneo Island. *Jurnal Meteorologi dan Geofisika*, 25(2), 83-92.

Benevides, P., Catalao, J., & Miranda, P. M. A. (2015). On the inclusion of GPS precipitable water vapour in the nowcasting of rainfall. *Natural Hazards and Earth System Sciences*, *15*(12), 2605–2616. doi: 10.5194/nhess-15-2605-2015

Bevis, M., Businger, S., Herring, T. A., Rocken, C., Anthes, R. A., & Ware, R. H. (1992). GPS meteorology: Remote sensing of atmospheric water vapor using the global positioning system. *Journal of Geophysical Research: Atmospheres*, 97(D14), 15787–15801. doi: 10.1029/92JD01517

BIG. (2025). *Sistem Referensi Geospasial Indonesia*. Badan Informasi Geospasial. Retrieved From https://srgi.big.go.id/

BMKG. (2025). *Data Online BMKG*. Badan Meteorologi, Klimatologi, Dan Geofisika. Retrieved From https://dataonline.bmkg.go.id/

BNPB. (2025). *Data Informasi Bencana Indonesia*. Badan Nasional Penanggulangan Bencana. Retrieved From https://dibi.bnpb.go.id/superset/dashboard/2/

Campos, T. B., Sapucci, L. F., Eichholz, C., Machado, L. A. T., & Adams, D. K. (2023). The Sensitivityof GPS Precipitable Water Vapor Jumps to Intense Precipitation Associated with Tropical Organized Convective Systems. *Atmosphere*, 14(2).doi: 1 0.3390/atmos14020262

Chen, B., & Liu, Z. (1955). Journal of geophysical research. *Nature*, 175(4449), 238. doi: 10.1038/175238c0

Chen, H., Xu, W., Liu, N., Sun, J., & Fu, J. (2022). Climatologies of Mesoscale Convective Systems over China Observed by Spaceborne Radars. *Monthly Weather Review*, 150(10), 2697–2717. doi: 10.1175/MWR-D-22-0002.1

Cheng, Y. M., Dias, J., Kiladis, G., Feng, Z., & Leung, L. R. (2023). Mesoscale Convective Systems Modulated by Convectively Coupled Equatorial Waves. *Geophysical Research Letters*, 50(10), 1–12. doi: 10.1029/2023GL103335

Crook, J., Morris, F., Fitzpatrick, R. G. J., Peatman, S. C., Schwendike, J., Stein, T. H., Birch, C. E., Hardy, S., & Yang, G. Y. (2024). Impact of the Madden–Julian oscillation and equatorial waves on tracked mesoscale convective systems over southeast Asia. *Quarterly Journal of the Royal Meteorological Society*, 150(760), 1724–1751. doi: 10.1002/qj.4667

Davis, J. L., Herring, T. A., Shapiro, I. I., Rogers, A. E. E., & Elgered, G. (1985). Geodesy by radio interferometry: Effects of atmospheric modeling errors on estimates of baseline length. *Radio Science*, 20(6), 1593–1607. doi: 10.1029/RS020i006p01593

Ding, T., Zhou, T., Guo, Z., Yang, Y., Zou, L., & Chen, X. (2024). Contribution of Mesoscale Convective Systems to Floods in the East Asian Summer Monsoon Region. *Geophysical Research Letters*, 51(13). doi: 10.1029/2023GL108125

Djakouré, S., Amouin, J., Kouadio, K. Y., & Kacou, M. (2024). Mesoscale Convective Systems and Extreme Precipitation on the West African Coast Linked to Ocean–Atmosphere Conditions during the Monsoon Period in the Gulf of Guinea. *Atmosphere*, 15(2). doi: 10.3390/atmos15020194

Drissi El Bouzaidi, R., El Talibi, H., El Moussaoui, S., & Mourabit, T. (2025). Estimating atmospheric precipitable water vapor in northern Morocco: A ground-based GNSS approach. *Scientific African*, 28, e02681. doi: 10.1016/j.sciaf.2025.e02681

Du, X., Sun, T., & Oo, K. T. (2025). Spatiotemporal Characteristics of Mesoscale Convective Systems in the Yangtze River Delta Urban Agglomeration and Their Response to Urbanization. *Atmosphere*, 16(3), 1–17. doi: 10.3390/atmos16030245

ECMWF. (2025). *ERA5 Hourly Data on Pressure Levels from 1940 to Present*. European Centre for Medium-Range Weather Forecasts. Retrieved From https://cds.climate.copernicus.eu/

Een Lujainatul Isnaini, Hafiz Mardian Abdussalam, Redho Surya Perdana, Akbar Wahyu Nugraha, & Aulia Try Atmojo. (2025). Determination of Zenith Tropospheric Delay (ZTD) Using CORS GNSS Data, 2016 – 2020 In Lampung. *Jurnal Inotera*, 10(2), 346–354. doi: 10.31572/inotera.vol10.iss2.2025.id520

Febrizky, L., Fadli, M., & Wiliam, W. (2023). Identifikasi Mesoscale Convective Complex (Mcc) Berbasis Data Satelit Himawari-8 Di Pulau Papua Dan Sekitarnya Desember 2021-November 2022. *OPTIKA: Jurnal Pendidikan Fisika*, 7(2), 294–305. doi: 10.37478/optika.v7i2.3132

Feng, Z., Hardin, J., Barnes, H. C., Li, J., Leung, L. R., Varble, A., & Zhang, Z. (2023). PyFLEXTRKR: a flexible feature tracking Python software for convective cloud analysis. *Geoscientific Model Development*, 16(10), 2753–2776. doi: 10.5194/gmd-16-2753-2023

Geng, J., Chen, X., Pan, Y., Mao, S., Li, C., Zhou, J., & Zhang, K. (2019). PRIDE PPP-AR: an open-source software for GPS PPP ambiguity resolution. *GPS Solutions*, 23(4), 91. doi: 10.1007/s10291-019-0888-1

Harjana, T., Hermawan, E., Risyanto, Purwaningsih, A., Andarini, D. F., Ridho, A., Ratri, D. N., & Sujalu, A. P. (2023). Meteorological Factors Influencing Coastal Flooding in Semarang, Central Java, Indonesia, on 23 May 2022. *Springer Proceedings in Physics*, 290, 259–267. doi: 10.1007/978-981-19-9768-6_25

Hermawan, E., Risyanto, R., Purwaningsih, A., Ratri, D. N., Ridho, A., Harjana, T., Andarini, D. F., Satyawardhana, H., & Sujalu, A. P. (2025). Characteristics of Mesoscale Convective Systems and Their Impact on Heavy Rainfall in Indonesia's New Capital City, Nusantara, in March 2022. *Advances in Atmospheric Sciences*, 42(2), 342–356. doi: 10.1007/s00376-024-4102-1

Huffman, G. J., Stocker, E. F., Bolvin, D. T., Nelkin, E. J., & Tan, J. (2023). *GPM IMERG Final Precipitation L3 Half Hourly 0.1 degree x 0.1 degree V07*. Goddard Earth Sciences Data and Information Services Center (GES DISC). Retrieved From https://doi.org/10.5067/GPM/IMERG/3B-HH/06

Ismanto, H. (2011). Karakteristik Kompleks Konvektif Skala Meso di Benua Maritim. *Tesis Institut Teknologi Bandung*.

Janowiak, J., Joyce, B., & Xie, P. (2017). *NCEP/CPC L3 Half Hourly 4km Global (60S - 60N) Merged IR V1*. Goddard Earth Sciences Data and Information Services Center (GES DISC). 10.5067/P4HZB9N27EKU

Jiang, P., Ye, S., Chen, D., Liu, Y., & Xia, P. (2016). Retrieving precipitablewater vapor data using GPS zenith delays and global reanalysis data in China. *Remote Sensing*, 8(5). doi: 10.3390/rs8050389

Jin, D., Oreopoulos, L., Lee, D., Tan, J., & Cho, N. (2021). Cloud–Precipitation Hybrid Regimes and Their Projection onto IMERG Precipitation Data. *Journal of Applied Meteorology and Climatology*, 60(6), 733–748. doi: 10.1175/JAMC-D-20-0253.1

Joyce, R. J., & Xie, P. (2011). Kalman Filter–Based CMORPH. *Journal of Hydrometeorology*, 12(6), 1547–1563. doi: 10.1175/JHM-D-11-022.1

Landskron, D., & Böhm, J. (2018). VMF3/GPT3: refined discrete and empirical troposphere mapping functions. *Journal of Geodesy*, 92(4), 349–360. doi: 10.1007/s00190-017-1066-2

Lian, D., He, Q., Li, L., Zhang, K., Fu, E., Li, G., Wang, R., Gao, B., & Song, K. (2023). A Novel Method for Monitoring Tropical Cyclones' Movement Using GNSS Zenith Tropospheric Delay. *Remote Sensing*, 15(13). doi: 10.3390/rs15133247

Maddox, R. A. (1980). Meoscale Convective Complexes. *Bulletin of the American Meteorological Society*, 61(11), 1374–1387. doi: 10.1175/1520-0477(1980)061<1374:mcc>2.0.co;2

Minnett, P. J., & Barton, I. J. (2010). Chapter 6 - Remote Sensing of the Earth's Surface Temperature. In Z. M. Zhang, B. K. Tsai, & G. B. T.-E. M. in the P. S. Machin (Eds.), *Radiometric Temperature Measurements: II. Applications* 43, 333–391. doi: 10.1016/S1079-4042(09)04306-9

Moker, J. M., Castro, C. L., Arellano, A. F., Serra, Y. L., & Adams, D. K. (2018). Convective-permitting hindcast simulations during the North American Monsoon GPS Transect Experiment 2013: Establishing baseline model performance without data assimilation. *Journal of Applied Meteorology and Climatology*, 57(8), 1683–1710. doi: 10.1175/JAMC-D-17-0136.1

Nuryanto, D. E., Hidayat, R., Pawitan, H., & Aldrian, E. (2018). The evolution of Mesoscale Convective System (MCS) around the Greater Jakarta area on 9 February 2015 using MTSAT Satellite. *Proceedings - 39th Asian Conference on Remote Sensing: Remote Sensing Enabling Prosperity, ACRS 2018*, 4, 2430–2438.

Nuryanto, D. E., Pawitan, H., Hidayat, R., & Aldrian, E. (2018). Kinematic and Thermodynamic Structures of Mesoscale Convective Systems During Heavy Rainfall in Greater Jakarta. *Makara Journal of Science*, 22(3). doi: 10.7454/mss.v22i3.8291

Nuryanto, D. E., Pawitan, H., Hidayat, R., & Aldrian, E. (2019). Characteristics of two mesoscale convective systems (MCSs) over the Greater Jakarta: case of heavy rainfall period 15–18 January 2013. *Geoscience Letters*, 6(1), 1–15. doi: 10.1186/s40562-019-0131-5

Nuryanto, D. E., Pawitan, H., Hidayat, R., & Aldrian, E. (2021). The occurrence of the typical mesoscale convective system with a flood-producing storm in the wet season over the Greater Jakarta area. *Dynamics of Atmospheres and Oceans*, 96(2), 101246. doi: 10.1016/j.dynatmoce.2021.101246

Pilewskie, J., & L'Ecuyer, T. (2025). The Role of Convective Intensity in Modulating the Earth's Radiative Balance. *Journal of Climate*, 1–44. doi: 10.1175/jcli-d-24-0334.1

Prein, A. F., Feng, Z., Fiolleau, T., Moon, Z. L., Núñez Ocasio, K. M., Kukulies, J., Roca, R., Varble, A. C., Rehbein, A., Liu, C., Ikeda, K., Mu, Y., & Rasmussen, R. M. (2024). Km-Scale Simulations of Mesoscale Convective Systems Over South America—A Feature Tracker Intercomparison. *Journal of Geophysical Research: Atmospheres*, 129(8), 1–25. doi: 10.1029/2023JD040254

Putri, N. S., Hayasaka, T., & Whitehall, K. D. (2017). The properties of mesoscale convective systems in Indonesia detected using the grab 'em tag 'em graph 'em (GTG) algorithm. *Journal of the Meteorological Society of Japan*, 95(6), 391–409. doi: 10.2151/jmsj.2017-026

Rais, A. F., Yunita, R., & Hananto, T. S. (2021). Pengaruh Mesoscale Convective System terhadap Hujan Ekstrem Pesisir Barat Sumatra. *Majalah Geografi Indonesia*, 35(1), 9. doi: 10.22146/mgi.60598

Raj, P. E., Devara, P. C. S., Maheskumar, R. S., Pandithurai, G., Dani, K. K., Saha, S. K., Sonbawne, S. M., & Tiwari, Y. K. (2004). Results of sun photometer-derived precipitable water content over a tropical Indian station. *Journal of Applied Meteorology*, 43(10), 1452–1459. doi: 10.1175/jam2149.1

Rajagopal, M., Russell, J., Skok, G., & Zipser, E. (2023). Tracking Mesoscale Convective Systems in IMERG and Regional Variability of Their Properties in the Tropics. *Journal of Geophysical Research: Atmospheres*, 128(24), 1–23. doi: 10.1029/2023JD038563

Ramos-Pérez, O., Adams, D. K., Ochoa-Moya, C. A., & Quintanar, A. I. (2022). A Climatology of Mesoscale Convective Systems in Northwest Mexico during the North American Monsoon. *Atmosphere*, 13(5), 1–27. doi: 10.3390/atmos13050665

Risanto, C. B., Castro, C. L., Arellano, A. F., Moker, J. M., & Adams, D. K. (2021). The impact of assimilating gps precipitable water vapor in convective-permitting wrf-arw on north american monsoon precipitation forecasts over northwest mexico. *Monthly Weather Review*, 149(9), 3013–3035. doi: 10.1175/MWR-D-20-0394.1

Risanto, C. B., Moker, J. M., Arellano, A. F., Castro, C. L., Serra, Y. L., Luong, T. M., & Adams, D. K. (2023). On the Collective Importance of Model Physics and Data Assimilation on Mesoscale Convective System and Precipitation Forecasts over Complex Terrain. *Monthly Weather Review*, 151(8), 1993–2008. doi: 10.1175/MWR-D-22-0221.1

Rustiana, S., Trismidianto, & Satyawardhana, H. (2019). The Influence of ENSO and IOD during Mesoscale Convective Complex (MCC) to Rainfall in Indonesia. *IOP Conference Series: Earth and Environmental Science*, 303(1). doi: 10.1088/1755-1315/303/1/012006

Saxena, S., & Dwivedi, R. (2023). An ERA5 based local modelling of weighted mean temperature over hilly region in India for improved spatiotemporal analysis of extreme weather event using GNSS PWV. *Advances in Space Research*, 72(8), 3022–3036. doi: 10.1016/j.asr.2023.06.017

Shohan, S., Koch, S. E., Castro, C. L., Arellano, A. F., Kay, J., Risanto, C. B., Weckwerth, T. M., Pinto, J. O., & Adams, D. K. (2025). Impact of Assimilating GPS Precipitable Water Vapor on Simulations of Two North American Monsoon Convective Events Using Observing System Simulation Experiments. *Journal of Geophysical Research: Atmospheres*, 130(16). https://doi.org/10.1029/2025JD044491

Shoji, Y. (2013). Retrieval of water vapor inhomogeneity using the japanese nationwide GPS array and its potential for prediction of convective precipitation. *Journal of the Meteorological Society of Japan*, 91(1), 43–62. doi: 10.2151/jmsj.2013-103

Stephens, G. L., Shiro, K. A., Hakuba, M. Z., Takahashi, H., Pilewskie, J. A., Andrews, T., Stubenrauch, C. J., & Wu, L. (2024). Tropical Deep Convection, Cloud Feedbacks and Climate Sensitivity. *Surveys in Geophysics*, 45(6), 1903–1931. doi: 10.1007/s10712-024-09831-1

Tai, S. L., Feng, Z., Marquis, J., & Fast, J. (2024). Characterizing Wet Season Precipitation in the Central Amazon Using a Mesoscale Convective System Tracking Algorithm. *Journal of Geophysical Research: Atmospheres*, 129(19). doi: 10.1029/2024JD041004

Trismidianto, Satiadi, D., Harjupa, W., Fathrio, I., Risyanto, Saufina, E., Muharsyah, R., Nuryanto, D. E., Nauval, F., Andarini, D. F., Purwaningsih, A., Harjana, T., Praja, A. S., Witono, A., Juaeni, I., & Suhandi, B. (2024). Southerly Surge Impact on Rainfall Patterns in Southern Indonesia during Winter Monsoon and Madden–Julian Oscillation (MJO). *Atmosphere*, 15(7). doi: 10.3390/atmos15070840

Trismidianto, & Satyawardhana, H. (2018). Mesoscale Convective Complexes (MCCs) over the Indonesian Maritime Continent during the ENSO events. *IOP Conference Series: Earth and Environmental Science*, 149(1). doi: 10.1088/1755-1315/149/1/012025

Wang, J., Fan, J., & Feng, Z. (2023). Climatological occurrences of hail and tornadoes associated with mesoscale convective systems in the United States. *Natural Hazards and Earth System Sciences*, 23(12), 3823–3838. doi: 10.5194/nhess-23-3823-2023

Wang, S., Xu, T., Nie, W., Jiang, C., Yang, Y., Fang, Z., Li, M., & Zhang, Z. (2020). Evaluation of precipitablewater vapor from five reanalysis products with ground-based GNSS observations. *Remote Sensing*, 12(11). doi: 10.3390/rs12111817

Wang, Z., & Yuan, J. (2025). A Novel Thermodynamical Predictor of Tropical High-Cloud Area Coverage: Estimated Anvil-Outflow Stability. *Geophysical Research Letters*, 52(11). doi: 10.1029/2025GL115026

Whitehall, K., Mattmann, C. A., Jenkins, G., Rwebangira, M., Demoz, B., Waliser, D., Kim, J., Goodale, C., Hart, A., Ramirez, P., Joyce, M. J., Boustani, M., Zimdars, P., Loikith, P., & Lee, H. (2015a). Exploring a graph theory based algorithm for automated identification and characterization of large mesoscale convective systems in satellite datasets. *Earth Science Informatics*, 8(3), 663–675. doi: 10.1007/s12145-014-0181-3

Whitehall, K., Mattmann, C. A., Jenkins, G., Rwebangira, M., Demoz, B., Waliser, D., Kim, J., Goodale, C., Hart, A., Ramirez, P., Joyce, M. J., Boustani, M., Zimdars, P., Loikith, P., & Lee, H. (2015b). Exploring a graph theory

based algorithm for automated identification and characterization of large mesoscale convective systems in satellite datasets. *Earth Science Informatics*, 8(3), 663–675. doi: 10.1007/s12145-014-0181-3

Xu, Y., Chen, X., Liu, M., Wang, J., Zhang, F., Cui, J., & Zhou, H. (2022). Spatial–Temporal Relationship Study between NWP PWV and Precipitation: A Case Study of 'July 20' Heavy Rainstorm in Zhengzhou. *Remote Sensing*, 14(15). doi: 10.3390/rs14153636

Yoshida, S., Sakai, T., Nagai, T., Seko, H., Kato, T., Shiraishi, K., & Shimizu, S. (2025). Observation of a slanted moisture structure with weak updraft leading to localized heavy rainfalls. *Scientific Reports*, 15(1), 1–9. doi: 10.1038/s41598-025-02314-2

Zhang, Y., Cai, C., Chen, B., & Dai, W. (2019). Consistency Evaluation of Precipitable Water Vapor Derived From ERA5, ERA-Interim, GNSS, and Radiosondes Over China. *Radio Science*, 54(7), 561–571. doi: 10.1029/2018RS006789